Monthly climatologies of zonal-mean and tidal winds in the thermosphere as observed by ICON/MIGHTI during April 2020–March 2022

Y. Yamazaki[1], B. J. Harding[2], L. Qiu[1,3], C. Stolle[1], T. A. Siddiqui[1], Y. Miyoshi[4], C. R. Englert[5], and S. L. England[6]

[1]Leibniz Institute of Atmospheric Physics at the University of Rostock, Kühlungsborn, Germany.
[2]Space Sciences Laboratory, University of California, Berkeley, CA, USA
[3]Institute of Geophysics and Geomatics, China University of Geosciences, Wuhan, China
[4]Department of Earth and Planetary Sciences, Kyushu University, Fukuoka, Japan
[5]Space Science Division, U.S. Naval Research Laboratory, Washington, DC, USA
[6]Virginia Polytechnic Institute and State University, Blacksburg, VA, USA

Key Points:

- Monthly climatologies of zonal-mean winds and tides at 90–110 km and 200–300 km are determined using v05 ICON/MIGHTI observations.
- ICON/MIGHTI and HWM14 results are in general agreement, providing a validation of the v05 ICON/MIGHTI data.
- HWM14 reproduces the zonal-mean winds well, but often underestimates tidal amplitude.

Corresponding author: Yosuke Yamazaki, `yamazaki@iap-kborn.de`

Abstract

Version 5 (v05) of the thermospheric wind data from the Michelson Interferometer for Global High-resolution Thermospheric Imaging (MIGHTI) instrument on the Ionospheric Connection Explorer (ICON) mission has been recently released, which largely avoids local-time dependent artificial baseline drifts that are found in previous versions of the ICON/MIGHTI wind data. This paper describes monthly climatologies of zonal-mean winds and tides based on the v05 ICON/MIGHTI data under geomagnetically quiet conditions (Hp30 < 3o) during April 2020–March 2022. Green-line winds in the lower thermosphere (90–110 km) and red-line winds in the middle thermosphere (200–300 km) are analyzed, as these data cover both daytime and nighttime. The altitude and latitude structures of zonal-mean winds and tides are presented for each month, and the results are compared with the widely-used empirical model, Horizontal Wind Model 2014 (HWM14). The v05 wind retrieval algorithm does not involve HWM14. The ICON/MIGHTI and HWM14 results are in general agreement, providing a validation of the v05 ICON/MIGHTI data. The agreement is especially good for the zonal-mean winds. The tidal amplitudes in HWM14 are often too small compared with those from ICON/MIGHTI as well as previous studies. A more accurate description of tides in the thermosphere is key to the future improvement of HWM.

1 Introduction

The uppermost layer of the Earth's atmosphere, the thermosphere, extends from ∼90 km up to ∼600 km (e.g., Richmond, 1983; Kato, 2007). Early studies evaluated densities of the thermosphere based on the measurement of orbital decay of artificial satellites. Jacchia (1965) developed a global empirical model of thermospheric densities under the assumption of diffusive equilibrium. A by-product of the model was an estimate of the global distribution of air pressure. Theoretical studies found that the model pressure provides useful information for evaluating the global wind system in the thermosphere (Geisler, 1967; Kohl & King, 1967). It has been demonstrated that global motion of the air above approximately 150 km is primarily driven by solar-induced pressure gradients. That is, horizontal winds blow from the higher-temperature (and higher-pressure) dayside to the lower-temperature (and lower-pressure) nightside. On the other hand, the motion of the air in the lower thermosphere (<150 km) is often dominated by waves from the lower layers of the atmosphere. In particular, atmopsheric tides (e.g., Lindzen

& Chapman, 1969) are known to play an important role for the meteorology of the mesosphere and lower thermosphere.

Theoretical models of the thermosphere were developed and used to explain how solar heating, as well as Joule heating in the polar region, drives the global circulation of the thermosphere under different seasonal conditions (e.g., Dickinson et al., 1975, 1977; Roble et al., 1977; Fuller-Rowell & Rees, 1980, 1981). These early modeling studies led to the development of upper atmosphere models that self-consistently couple the thermosphere and ionosphere (e.g., Roble et al., 1988; Richmond et al., 1992; Fuller-Rowell et al., 1994). Thermospheric winds can have a significant impact on ionospheric dynamics (e.g., Rishbeth, 1998) and electrodynamics (e.g., Heelis, 2004), and thus are important for the accurate description of space weather.

There are several ways to observe thermospheric winds. For instance, wind velocities can be measured using an accelerometer onboard a low-Earth-orbit satellite. Past satellite missions like Dynamic Explorer 2 (DE2) (Spencer et al., 1982), CHAllenging Minisatellite Payload (CHAMP) (H. Liu et al., 2006; Sutton et al., 2007), and Gravity Field and Steady State Ocean Circulation Explorer (GOCE) (Doornbos et al., 2010; H. Liu et al., 2016) provided global in-situ observations of thermospheric winds. Wind velocities can also be measured with a sounding rocket, which can reach the thermosphere. For example, the chemical release technique (e.g., Larsen, 2002; Pfaff et al., 2020) uses measurements of trails of a chemical tracer released by a rocket to derive thermospheric wind velocities. Moreover, optical measurements of Doppler shifts in airglow emissions, such as the 557.7 nm $O(^1S)$ green line and the 630.0 nm $O(^1D)$ red line, have also been used to observe thermospheric wind velocities from ground stations (e.g., Shiokawa et al., 1999; Meriwether, 2006; Makela et al., 2012) as well as from satellites such as DE2 (Hays et al., 1981), Upper Atmosphere Research Satellite (UARS) (Hays et al., 1993) and Thermosphere-Ionosphere-Mesosphere Energetics and Dynamics (TIMED) (Killeen et al., 2006). Ground-based meteor radars can be used to measure wind velocities in the mesosphere and lower thermosphere around 80–100 km (e.g., Hocking et al., 2001; Chau et al., 2019). Thermospheric wind velocities at E-region and F-region heights can also be estimated using incoherent scatter radar measurements of ionospheric parameters (e.g., Salah & Holt, 1974; Harper, 1977).

Global empirical models of thermospheric winds have been developed based on the measurements obtained through the techniques mentioned above and others. The most commonly used empirical model is the Horizontal Wind Model (HWM) series (e.g., Hedin et al., 1991, 1996; Drob et al., 2008, 2015). HWM is constructed by fitting analytical functions to a large volume of historical data. It predicts the zonal and meridional components of the neutral wind velocity at a given location (latitude, longitude and altitude) and time (day of year and UT). The latest version is HWM14 (Drob et al., 2015), and since its release, the model has been widely used in the space physics community. The validation of HWM is a community effort. Thermospheric wind measurements are often compared against HWM for a validation of the observational data as well as for a performance evaluation of HWM (e.g., Englert et al., 2012; Jiang et al., 2018; Li et al., 2021; Tang et al., 2021; Okoh et al., 2022). The present study shows comparisons of HWM14 with thermospheric wind observations from the Ionospheric Connection Explorer (ICON) mission, which was launched on October 11, 2019 (Immel et al., 2018).

The Michelson Interferometer for Global High-Resolution Thermospheric Imaging (MIGHTI) instrument onboard ICON measures the horizontal wind velocity by observing Doppler shifts of the atomic oxygen airglow emissions (e.g., Englert et al., 2017; Harding et al., 2017). The green-line wind measurements extend from an altitude of 90 km to 300 km during the daytime but to only 110 km at night, as the strength of the green-line emission varies considerably from day to night. The red-line wind data cover the height range approximately 160–300 km during day and 200–300 km at night. These wind data are useful not only for studying the neutral dynamics of the thermosphere (e.g., He et al., 2021; Cullens et al., 2020; Yiğit et al., 2022; Forbes et al., 2022; Englert et al., 2017; Triplett et al., 2023) but also for investigating atmosphere-ionosphere coupling processes, which can be realized by combining the ICON/MIGHTI wind data with ionospheric measurements made by ICON (e.g., England et al., 2021; Immel et al., 2021; Forbes et al., 2021; Park et al., 2021; Heelis et al., 2022; R. Zhang et al., 2022) or by other missions (e.g., Gasperini et al., 2021, 2022; G. Liu et al., 2021; Yamazaki et al., 2021; Yamazaki, Arras, et al., 2022; Aa et al., 2022; Le et al., 2022; Harding et al., 2022; Oberheide, 2022).

The studies mentioned above used version 4 (v04) or an earlier version of the ICON/MIGHTI wind data. The v04 wind data, especially during the early period of the mission, showed reasonable agreement with other independent observations (e.g., Harding et al., 2021; Makela et al., 2021; Dhadly et al., 2021; Chen et al., 2022). However, later it became clear that the baseline of the v04 data has slowly drifted over time, leading to errors of 50–100 m/s for some cases in 2021. This issue was described in detail by Englert et al. (2023). The baseline drift was found to be dependent on the local time and height, which has made the reliable assessment of zonal-mean winds and tides difficult. Version 5 (v05) of the ICON/MIGHTI wind data has been recently (in November 2022) released. A new calibration method for the so-called "zero wind" has been developed for v05, which uses a long-term comparison of the ascending- and descending-orbit data to perform a self-calibration of the zero baseline, independent of external data or models (Englert et al., 2023). The present study evaluates, for the first time, zonal-mean winds and tides using the v05 ICON/MIGHTI wind data for the height ranges 90–110 km and 200–300 km, where wind measurements are made during both day and night. Monthly climatologies derived from the ICON/MIGHTI observations during April 2020–March 2022 are compared with HWM14 predictions.

2 Method to Determine Zonal-mean Winds and Tides

The v05 ICON/MIGHTI wind data (level 2.2, cardinal vector winds) during the 24-month period from April 2020 to March 2022 are analyzed to determine zonal-mean winds and tides. The estimated accuracy of the v05 wind data is generally 10–25 m/s (Englert et al., 2023). Only the data that are flagged as "Good" (Wind_Quality = 1) are used. This largely eliminates (1) the observations from the South Atlantic Anomaly where the retrieval of wind velocities is difficult due to increased radiation, (2) the observations with little airglow signal, and (3) the observations from the day-night terminators where mode changes of the instrument take place. Cullens et al. (2020), using synthetic data sampled along the ICON/MIGHTI measurement points, demonstrated that (3) does not have a large impact on the estimation of tidal amplitude.

We use only the measurements made during geomagnetically quiet periods. Our criterion for the geomagnetically quiet periods is Hp30 < 3o, where Hp30 is the geomagnetic activity index described by Yamazaki, Matzka, et al. (2022). Briefly, Hp30 is a planetary geomagnetic activity index, similar to Kp (Matzka et al., 2021) but with a higher temporal resolution of 30 minutes in contrast to the 3-hourly Kp index. The higher temporal resolution has an advantage in accurately selecting quiet-time data. Hp30 is produced at the GeoForschungsZentrum (GFZ) Potsdam and distributed at their website: `https://kp.gfz-potsdam.de/en/hp30-hp60`.

The green-line winds are given at every ~3 km for the height range 91–112 km, while the red-line winds are given at every ~10 km for 203–301 km. At each height, the data were binned in hourly UT bins, in 5° latitude bins every 2.5° latitude from 10°S to 40°N, and in 15° longitude bins every 15° longitude. This was done separately for each month of the year (but without distinction of different years) and for the zonal and meridional components of the wind. The mean value and standard deviation were computed for each bin. The standard deviation is used, in a later step, to evaluate 1-σ uncertainties in zonal-mean winds and tides. The bin-mean values at given latitude and height were expressed as a function of UT (t in hours), longitude (λ in degrees), and month (M=1, 2, ..., 12) using the following analytical representation:

$$\sum_{n=0}^{4}\sum_{s=-4}^{4}\sum_{m=0}^{3}\left\{a_{nsm}\cos\left(n\frac{t}{24}-s\frac{\lambda}{360}+m\frac{M}{12}\right)+b_{nsm}\sin\left(n\frac{t}{24}-s\frac{\lambda}{360}+m\frac{M}{12}\right)\right\}. \quad (1)$$

Formula (1) takes into account zonal-mean winds, tides and stationary planetary waves, and their seasonal variations. n represents the tidal frequency. That is, n=1, 2, 3, 4 correspond to the 24-h (or diurnal) tide, 12-h (or semidiurnal) tide, 8-h (or terdiurnal) tide and 6-h tide, respectively. The higher order tides are generally not as important in the thermosphere (e.g., Oberheide et al., 2011). $|s|$ denotes the zonal wavenumber, and the sign of s indicates the direction of the zonal propagation of tides. That is, s>0 and s<0 correspond to eastward- and westward-propagating tides, respectively. The standard tidal nomenclature is used throughout this paper, such as DE3 and SW2, where the first letter indicates the period (i.e., “D” for diurnal and “S” for semidiurnal), the second letter represents the propagation direction (i.e., “E” for eastward and “W” for westward), and the last number is the zonal wavenumber $|s|$. Going back to formula (1), the zonal-mean winds are represented by the terms with n=0 and s=0, while stationary planetary waves are represented by the terms with n=0 and $|s|$>0. The seasonal variations of the zonal-mean winds, tides and stationary planetary waves are represented by m=1, 2, 3, corresponding to the annual, semiannual and terannual cycles. The coefficients a_{nsm} and b_{nsm} were determined in such a way that the deviation of formula (1) from the binned values of the ICON/MIGHTI data will be the smallest in a least-squares sense.

The goodness-of-fit was evaluated using two statistical metrics. One is the correlation coefficient between the observations (X) and fit (Y):

$$r=\frac{Cov\left(X,Y\right)}{\sqrt{Cov\left(X,X\right)Cov\left(Y,Y\right)}}, \quad (2)$$

where Cov is the covariance. The other is the root-mean-square error:

$$\mathrm{RMS} = \sqrt{\frac{\sum (X-Y)^2}{N}}, \tag{3}$$

where N is the number of the observations. The latitude and height distributions of the correlation coefficient and root-mean-square error are presented in Figure 1. The correlation coefficient is generally higher in the middle thermosphere (r=0.8–1.0, based on red-line winds) than in the lower thermosphere (r=0.65–0.85, based on green-line winds). This is mainly due to the fact that the lower thermosphere is more strongly influenced by the waves that are not described by formula (1) such as acoustic waves, gravity waves, lunar tides, Kelvin waves, and Rossby waves (e.g., Yiğit & Medvedev, 2015; H.-L. Liu, 2016). These waves are generated in the lower layers of the atmosphere and propagate into the thermosphere. They can interact with tides and other waves to produce secondary waves, which makes the spatial temporal variability of the lower thermosphere rather complex (e.g., Chang et al., 2011; H.-L. Liu, 2014; Nystrom et al., 2018). The waves from the lower atmosphere get strongly dissipated before reaching the middle thermosphere. The middle thermosphere is dominated by the diurnal tide that is locally generated by solar heating (Hagan et al., 2001), which can be represented well by formula (1). RMS is somewhat larger in the middle thermosphere (20–30 m/s) than in the lower thermosphere (15–25 m/s). This reflects generally larger wind velocities in the middle thermosphere. These RMS values are much smaller than those reported for HWM14 (40–80 m/s) by Drob et al. (2015). This is not surprising given that HWM14 involves more diverse sources of data from many different years with various degrees of accuracy.

For a given month M, formula (1) can be rewritten in the following form, which more explicitly represents the zonal-mean winds and waves:

$$\overline{A} + \sum_{n=1}^{4}\sum_{s=-4}^{4} A_{ns}\cos\left(n\frac{t}{24} - s\frac{\lambda}{360} + P_{ns}\right) + \sum_{s=1}^{4} A'_s \cos\left(s\frac{\lambda}{360} + P'_s\right). \tag{4}$$

Here, $\overline{A}$ is the zonal-mean wind velocity (in m/s), A_{ns} and P_{ns} are the amplitude (in m/s) and phase (in rad) of a tide, respectively. A'_s and P'_s are the amplitude and phase of a stationary planetary wave, respectively. 1-σ uncertainties in the zonal-mean winds, tides and stationary planetary waves were evaluated using the standard deviation obtained during the binning procedure described earlier. A Monte Carlo method was used for this purpose. That is, random noise was generated for each bin based on the standard deviation, and the noise was superimposed on the corresponding mean value. Fitting of

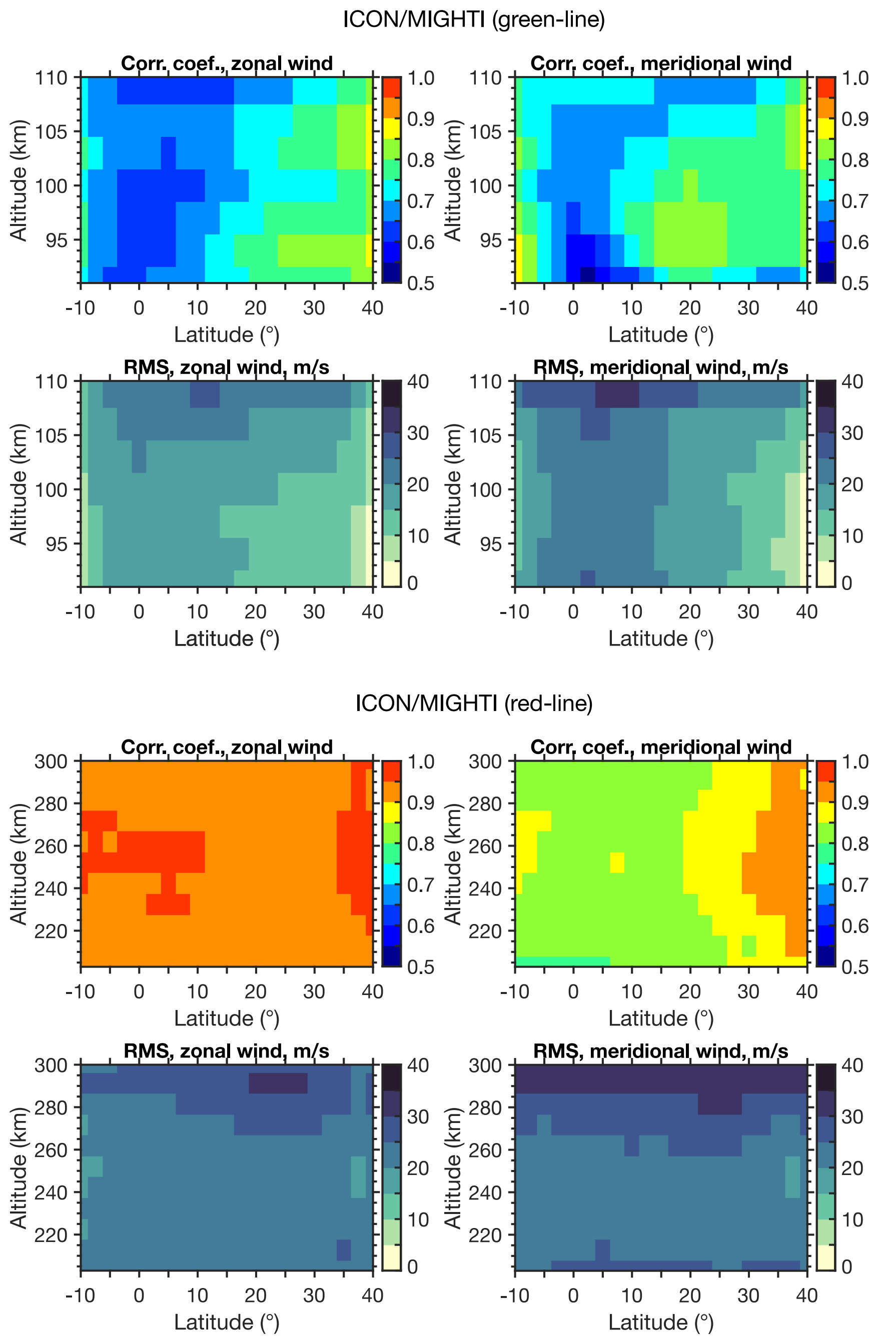

Figure 1. Correlation coefficient and root-mean-square error (RMS), as measures of goodness-of-fit of formula (1) to the v05 ICON/MIGHTI green-line data (top four panels) and red-line data (bottom four panels). The left and right panels are for the zonal and meridional winds, respectively.

formula (1) was repeated for 250 Monte Carlo samples, and 1-σ uncertainties were computed for the zonal-mean wind velocity, and the amplitude and phase of tides and stationary planetary waves at each latitude and height. The derived 1-σ uncertainty in the zonal-mean wind velocity is typically 1.0–3.5 m/s for both green-line and red-line winds. The 1-σ uncertainties in the amplitude and phase of tides and stationary planetary waves are typically less than 4.5 m/s and 20°, respectively. These uncertainty values are appreciably smaller compared to the features discussed in this paper.

Zonal-mean winds, tides and stationary planetary waves were also evaluated using HWM14 for the purpose of comparison. Hourly values of the zonal and meridional wind velocities were derived from HWM14 for each month by running the model for the 15th day of the month without including disturbance winds (Emmert et al., 2008). At each latitude and height, the zonal-mean wind velocity, and the amplitude and phase of tides and stationary planetary waves were determined by least-squares fitting of formula (4), which can be directly compared with the ICON/MIGHTI results.

3 Results

First, we examine seasonal climatologies of zonal-mean winds. Figure 2 depicts the zonal-mean zonal and meridional winds in the lower thermosphere (91–110 km) as derived from the ICON/MIGHTI green-line measurements. Below ∼105 km, the zonal-mean zonal wind in the equatorial region (10°S–10°N) tends to be weakly westward throughout the year. An eastward jet can be seen at 30°N during the Northern Hemisphere (N.H.) summer. The reversal of the zonal-mean zonal wind is often seen around 105 km, which was also noted by Yiğit et al. (2022). The zonal-mean meridional wind is generally weak with little seasonal variation. The corresponding results obtained from HWM14 are presented in Figure 3. HWM14 captures the salient features of the observed zonal-mean zonal and meridional winds well.

Figure 4 shows the zonal-mean zonal and meridional winds in the middle thermosphere (203–300 km) as derived from the ICON/MIGHTI red-line measurements. An annual variation of the zonal-mean zonal wind is evident. That is, the zonal wind in the N.H. is largely eastward and westward during the local winter and summer, respectively. The seasonal variation of the zonal-mean meridional wind is also dominated by an annual cycle. That is, the meridional wind is primarily northward during the N.H. winter

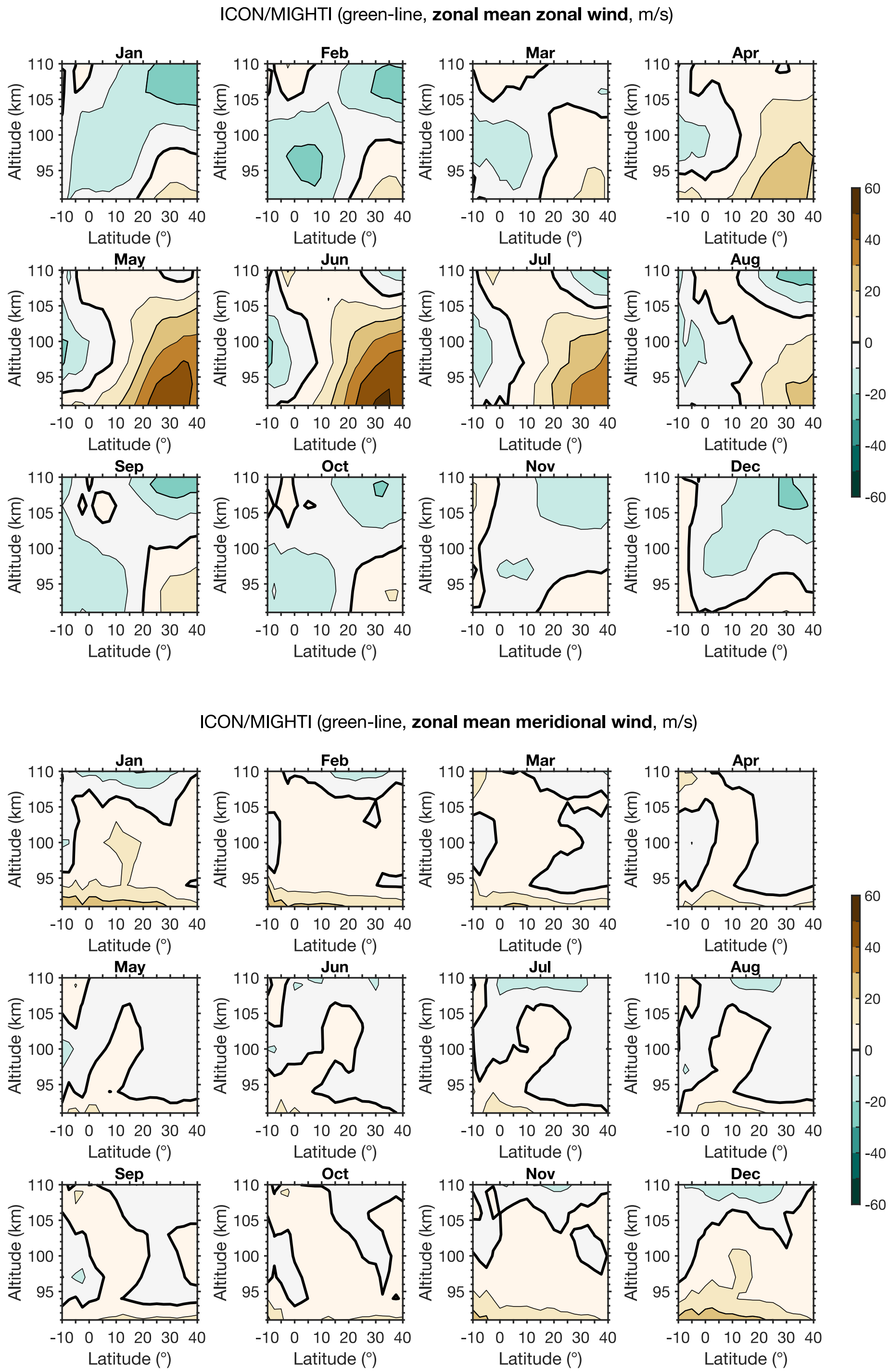

Figure 2. Quiet-time monthly climatologies of the zonal-mean zonal wind (top 12 panels) and zonal-mean meridional wind (bottom 12 panels) in the lower thermopshere (91–110 km) as derived from the v05 ICON/MIGHTI green-line data during April 2020–March 2022.

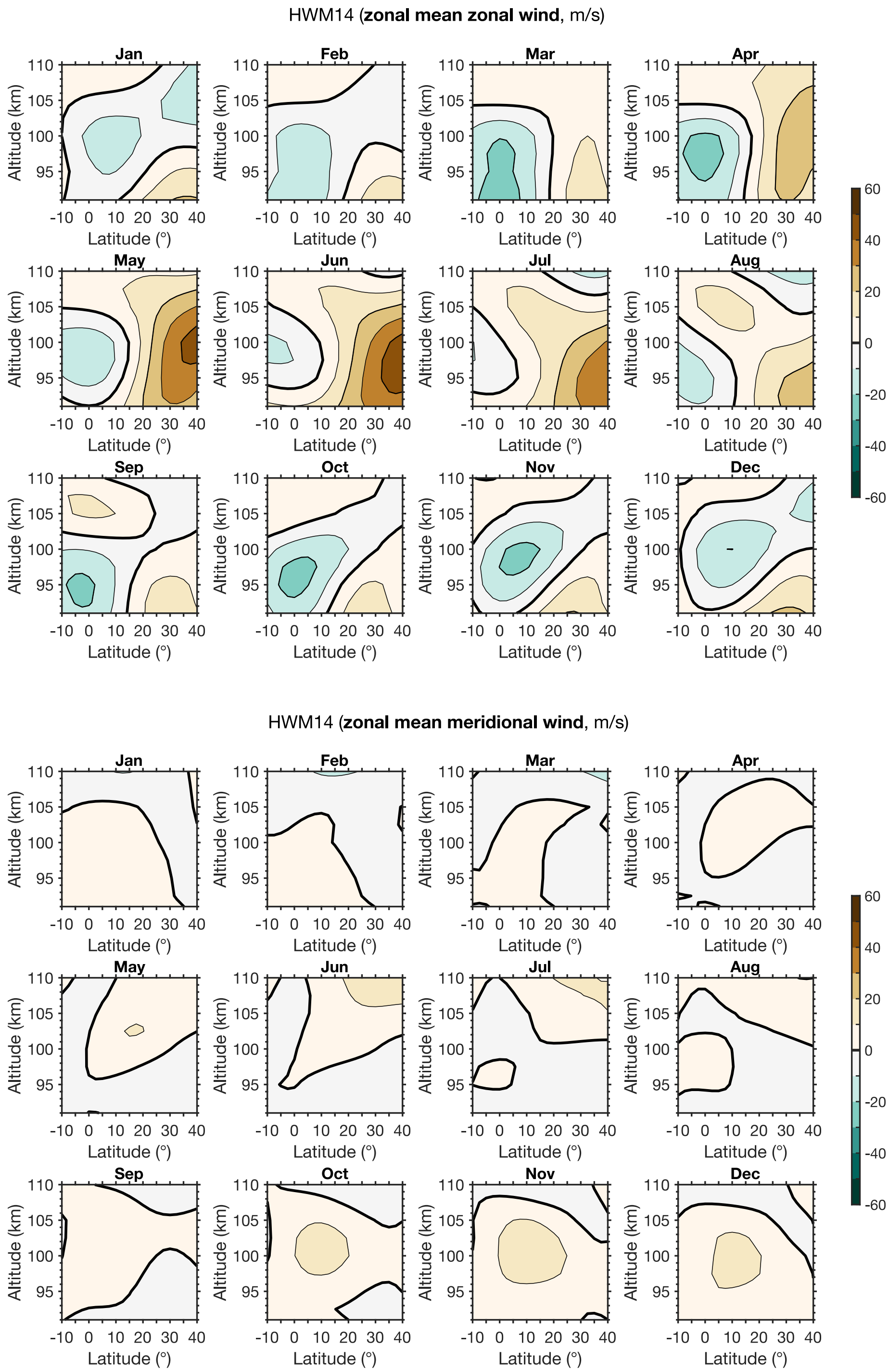

Figure 3. Same as Figure 2 but from Horizontal Wind Model 2014 (HWM14).

and southward during the N.H. summer. The seasonal transitions occur in March and September. The annual variations in the zonal-mean zonal and meridional winds are reproduced well by HWM14 as shown in Figure 5.

Next, we examine seasonal climatologies of tides and stationary planetary waves. Different components of waves, as expressed by different combinations of (n, s), have varying degrees of significance in the thermosphere (e.g., Truskowski et al., 2014; Forbes et al., 2014). Figures 6 and 7 depict wave spectra for two representative altitudes. Figure 6 shows the amplitude of different wave components for the green-line winds over the equator at an altitude of 106 km. At this particular latitude and height, the eastward-propagating diurnal tide with zonal wavenumber 3 (DE3; n=1, s=3) dominates the tide in the zonal wind, especially during July–November, and the migrating semidiurnal tide (SW2; n=2, s=−2) dominates the tide in the meridional wind, especially during April–September. Figure 7 is similar to Figure 6 but for the red-line winds at 30°N at an altitude of 273 km. In the middle thermosphere, the migrating diurnal tide (DW1; n=1, s=−1) is by far dominant. Since DW1, SW2 and DE3 are found to be dominant within the latitudinal and altitudinal range of the ICON/MIGHTI wind measurement, we further analyze these specific tides.

Figure 8 shows the amplitude and phase of DW1 in the meridional wind in the lower thermosphere as derived from the ICON/MIGHTI green-line measurements. The amplitude is largest at 15–20°N and 95–97 km, and it shows a semiannual variation with equinoctial maxima of ∼60 m/s. The phase of DW1 tends to decrease with increasing height. This 'downward phase propagation' is a fundamental feature of upward-propagating tides (e.g., Forbes, 1995). The results suggest that DW1 in the lower thermosphere originate from lower layers of the atmosphere. The latitude-height pattern of the DW1 phase does not vary much with the season. DW1 derived from HWM14 is presented in Figure 9. The DW1 amplitude in HWM14 is largest at 15–20°N, which is in agreement with the ICON/MIGHTI results. HWM14 also reproduces the semiannual variation in the DW1 amplitude. However, the DW1 amplitude in HWM14 is generally too small, and its height structure does not agree well with the observations. The latitude and height structures of the DW1 phase are reproduced by HWM14 during equinoctial months.

Figure 10 presents the SW2 amplitude and phase in the meridional wind in the lower thermosphere as derived from the ICON/MIGHTI green-line measurements. The am-

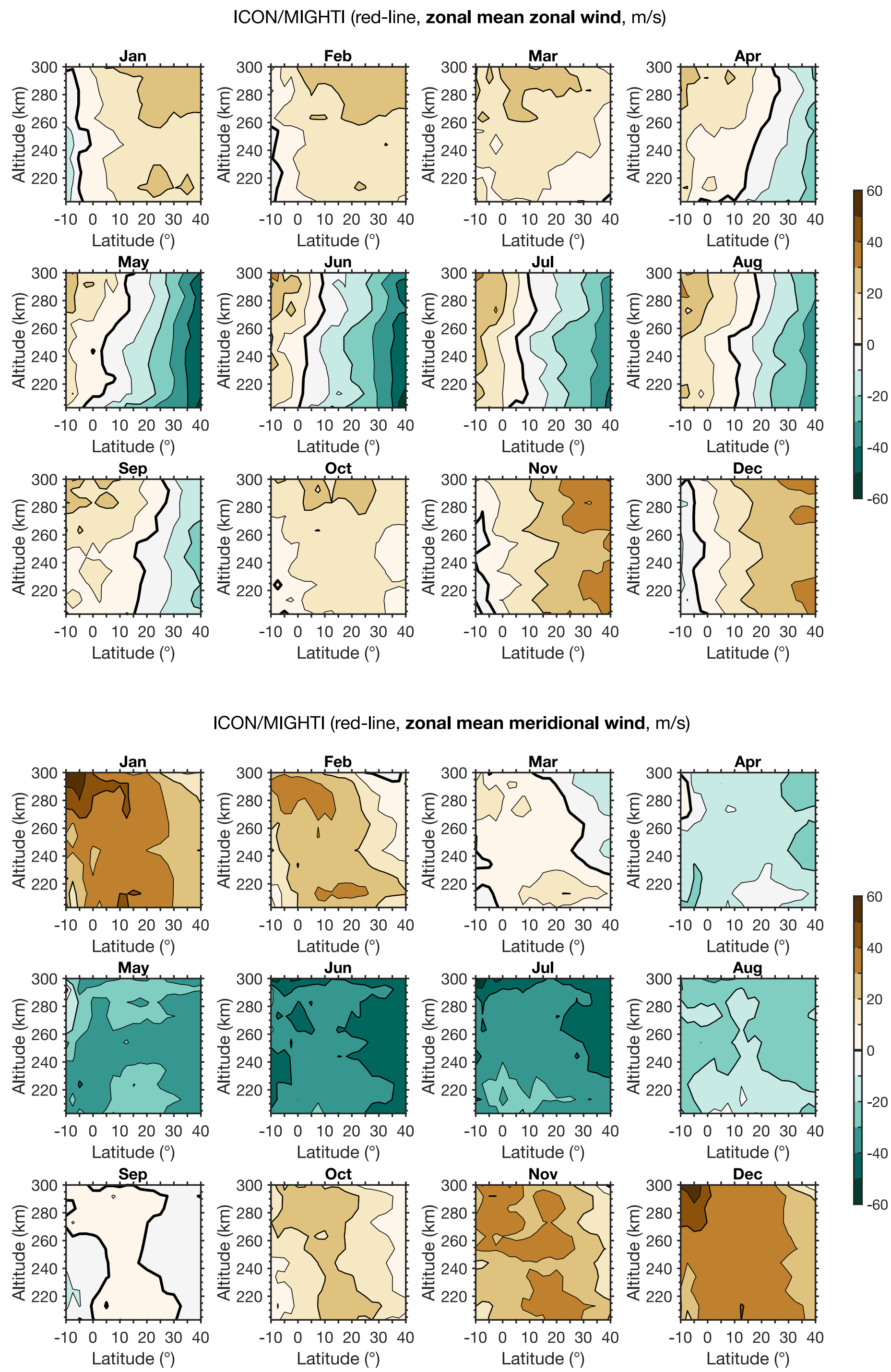

Figure 4. Quiet-time monthly climatologies of the zonal-mean zonal wind (top 12 panels) and zonal-mean meridional wind (bottom 12 panels) in the middle thermosphere (203–300 km) as derived from the v05 ICON/MIGHTI red-line data during April 2020–March 2022.

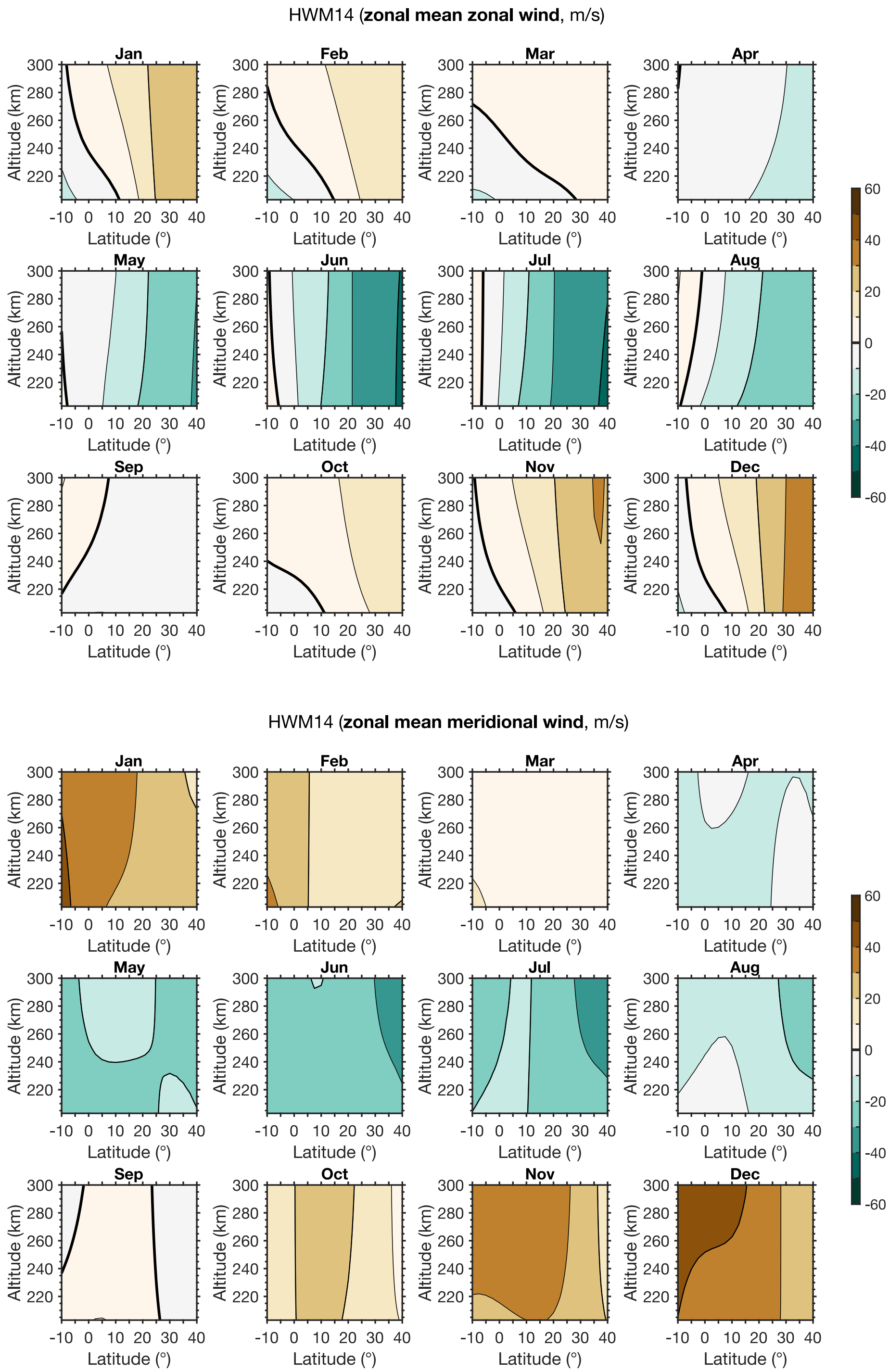

Figure 5. Same as Figure 4 but from Horizontal Wind Model 2014 (HWM14).

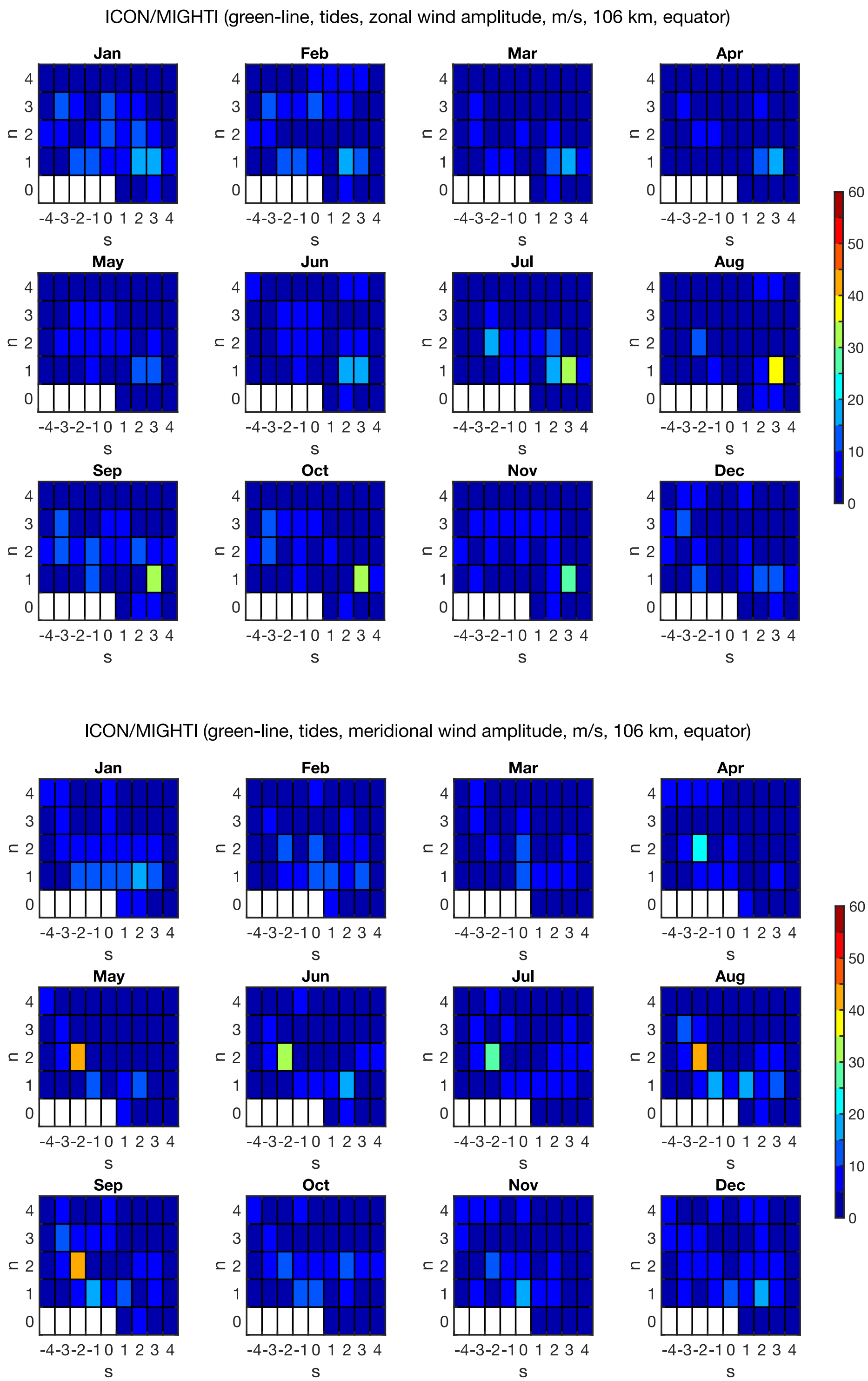

Figure 6. Amplitude of tides and stationary planetary waves in the zonal wind (top 12 panels) and meridional wind (bottom 12 panels) at 106 km at the equator as derived from the v05 ICON/MIGHTI green-line data. n represents tidal frequency. That is, n=1 for diurnal tides, n=2 for semidiurnal tides, and so on. n=0 for stationary planetary waves. s is the zonal wavenumber. s>0 for eastward-propagating waves, while s<0 for westward-propagating waves.

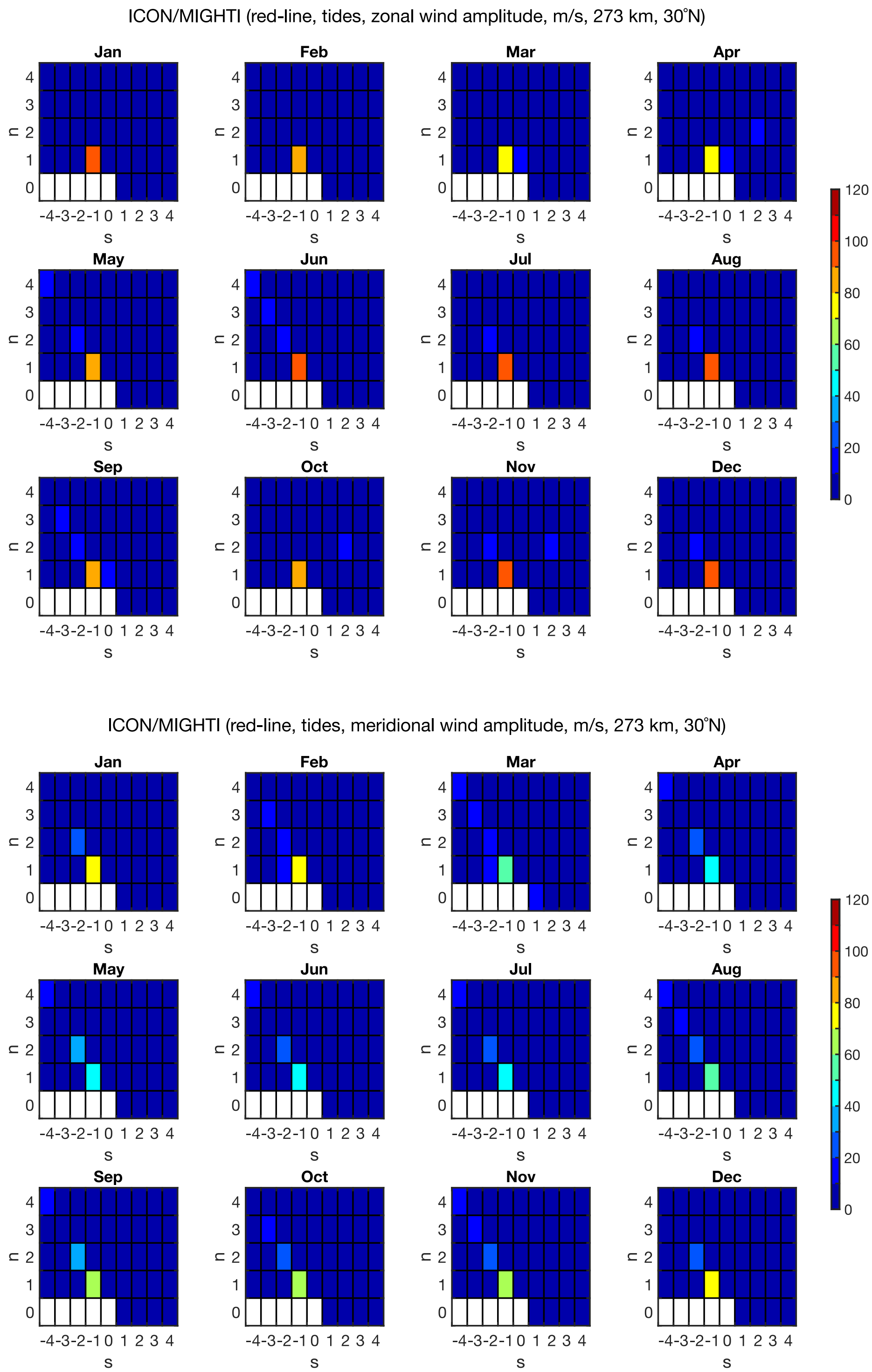

Figure 7. Same as Figure 6 but at 273 km at 30°N as derived from the v05 ICON/MIGHTI red-line data.

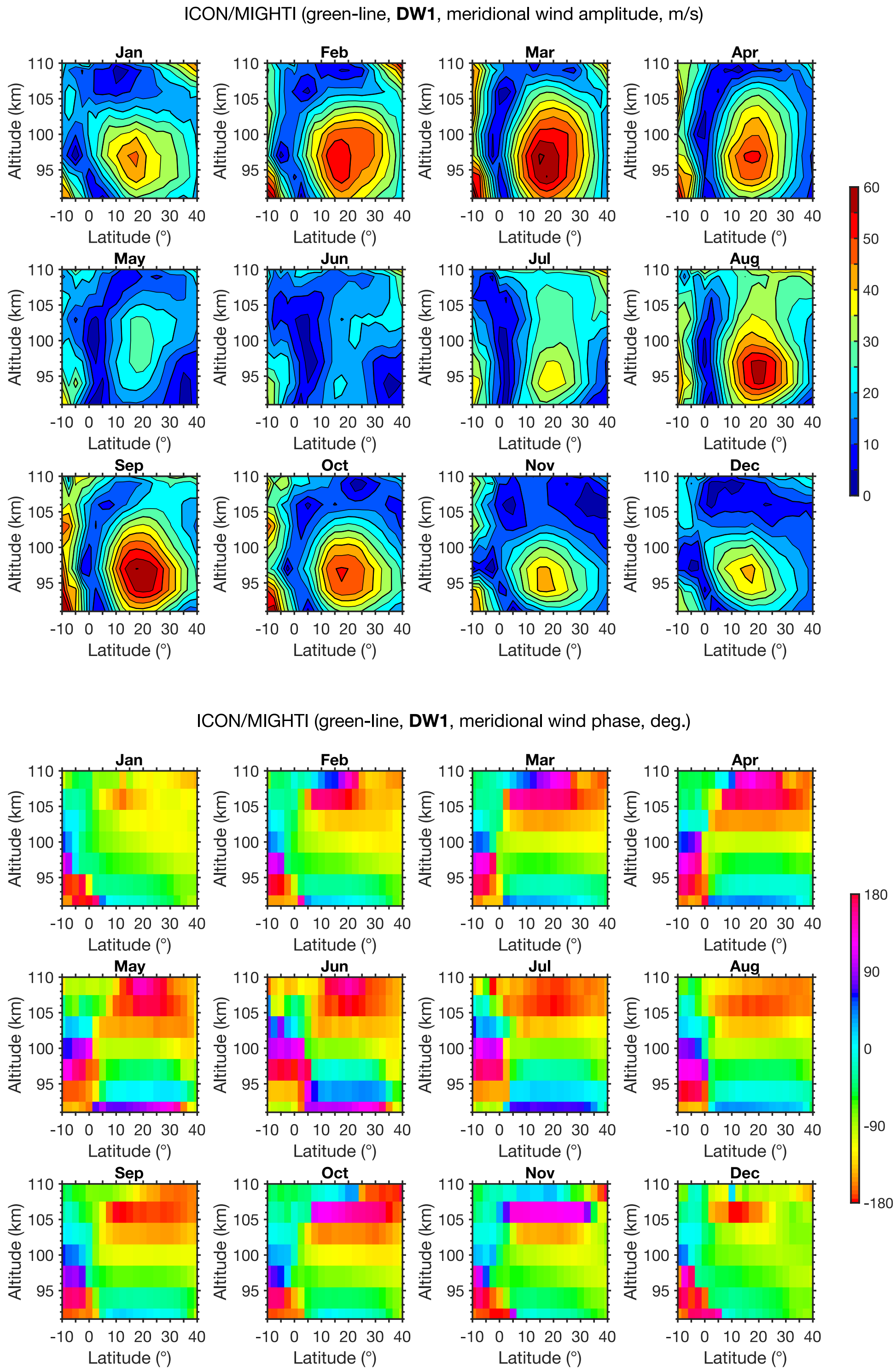

Figure 8. Amplitude (top 12 panels) and phase (bottom 12 panels) of the migrating diurnal tide (DW1) in the meridional wind in the lower thermosphere as derived from the v05 ICON/MIGHTI green-line data. The corresponding results for the zonal wind can be found in Figure S1 of Supporting Information.

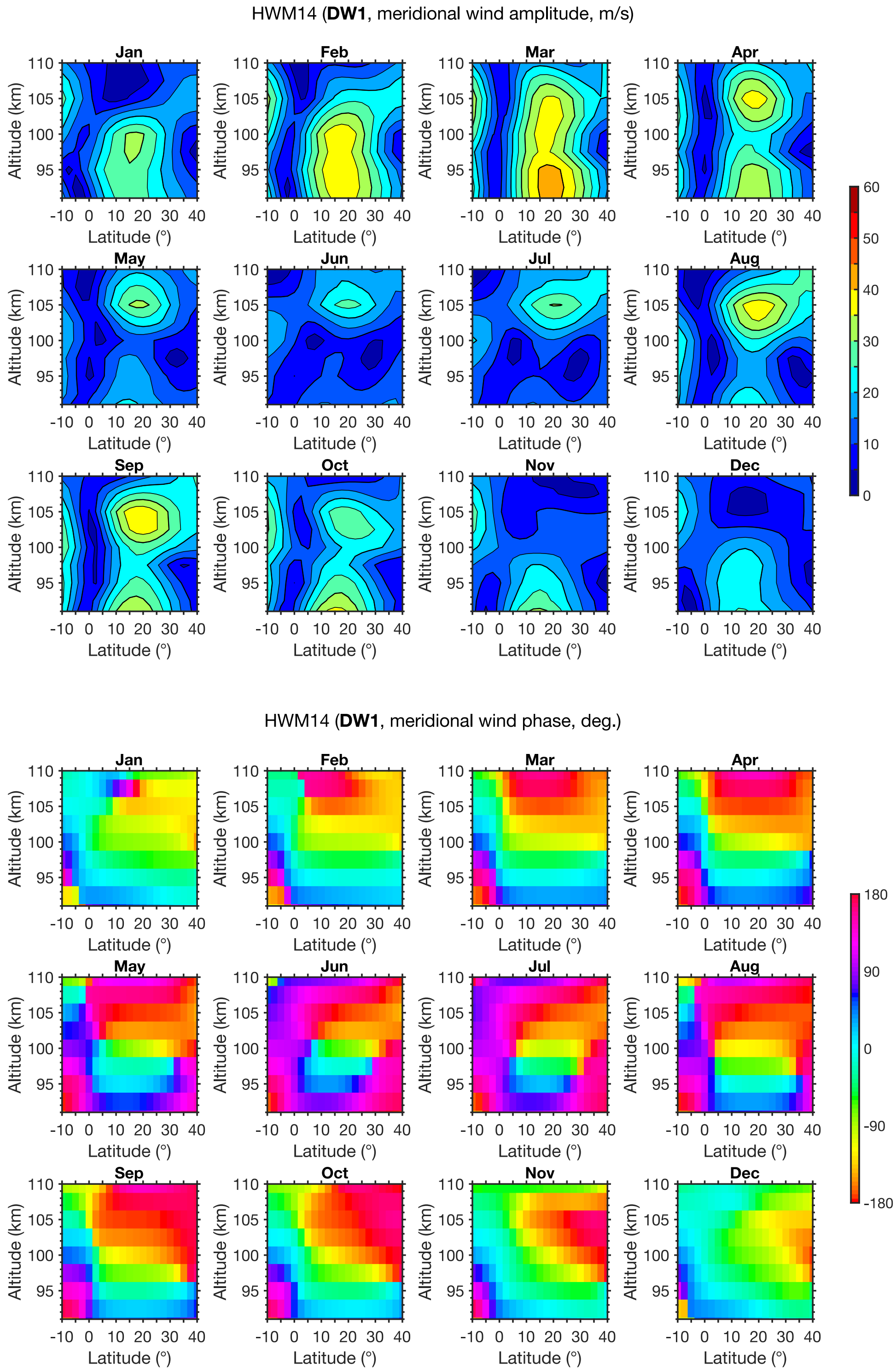

Figure 9. Same as Figure 8 but from Horizontal Wind Model 2014 (HWM14).

plitude is relatively large over the equator (10°S–10°N) and at N.H. middle latitudes (>30°N). In the equatorial region, the amplitude grows with height, reaching 60 m/s at 110 km during August–September. The maximum amplitude probably occurs above 110 km. At middle latitudes, the amplitude peaks at 105 km. The downward phase propagation is seen at both equatorial and middle-latitude regions, indicating that the SW2 energy propagates upward at these heights. The corresponding results derived from HWM14 are shown in Figure 11. Again, the amplitude in HWM14 is generally too small, and its height structure does not agree well with the observations. Interestingly, there is remarkable agreement in the phase of SW2 in the lower thermosphere between the ICON/MIGHTI and HWM14 results.

Figure 12 shows the amplitude and phase of DE3 in the zonal wind in the lower thermosphere as derived from the ICON/MIGHTI green-line measurements. DE3 is the largest non-migrating (i.e., non-sun-synchronous) tidal component found in the green-line data. The zonal-wind amplitude is largest over the equator at a height of 105–110 km. The maximum amplitude exceeds 30 m/s during July–October. The downward phase propagation is visible, indicating upward energy propagation of DE3. DE3 is nonexistent in HWM14, as the model does not take into account any non-migrating tide.

We now look at DW1 in the middle thermosphere. Figure 13 shows the amplitude and phase of DW1 in the zonal wind in the middle thermosphere as derived from the ICON/MIGHTI red-line observations. It is noted that the scale range for the amplitude is different from those used for the green-line results (Figures 8, 10 and 12). The DW1 amplitude grows with height from ∼50 m/s at 200 km to ∼90 m/s at 300 km. It exceeds 100 m/s in some months. The phase does not vary with height, indicating that DW1 in the middle thermosphere is a vertically-trapped (evanescent) tidal mode that is locally generated, rather than an upward-propagating mode from below. The corresponding results derived from HWM14 are presented in Figure 14. HWM14 reproduces the latitude and height structures of the amplitude and phase well. Figure 15 also shows the amplitude and phase of DW1 from the ICON/MIGHTI red-line measurements, but for the meridional wind. The amplitude is small over the equatorial region but can exceed 100 m/s at middle latitudes (>30°N) above 280 km. The phase depends strongly on latitude. The phase structure is well captured by HWM14 (Figure 16), but the model severely underestimates the DW1 amplitude at middle latitudes.

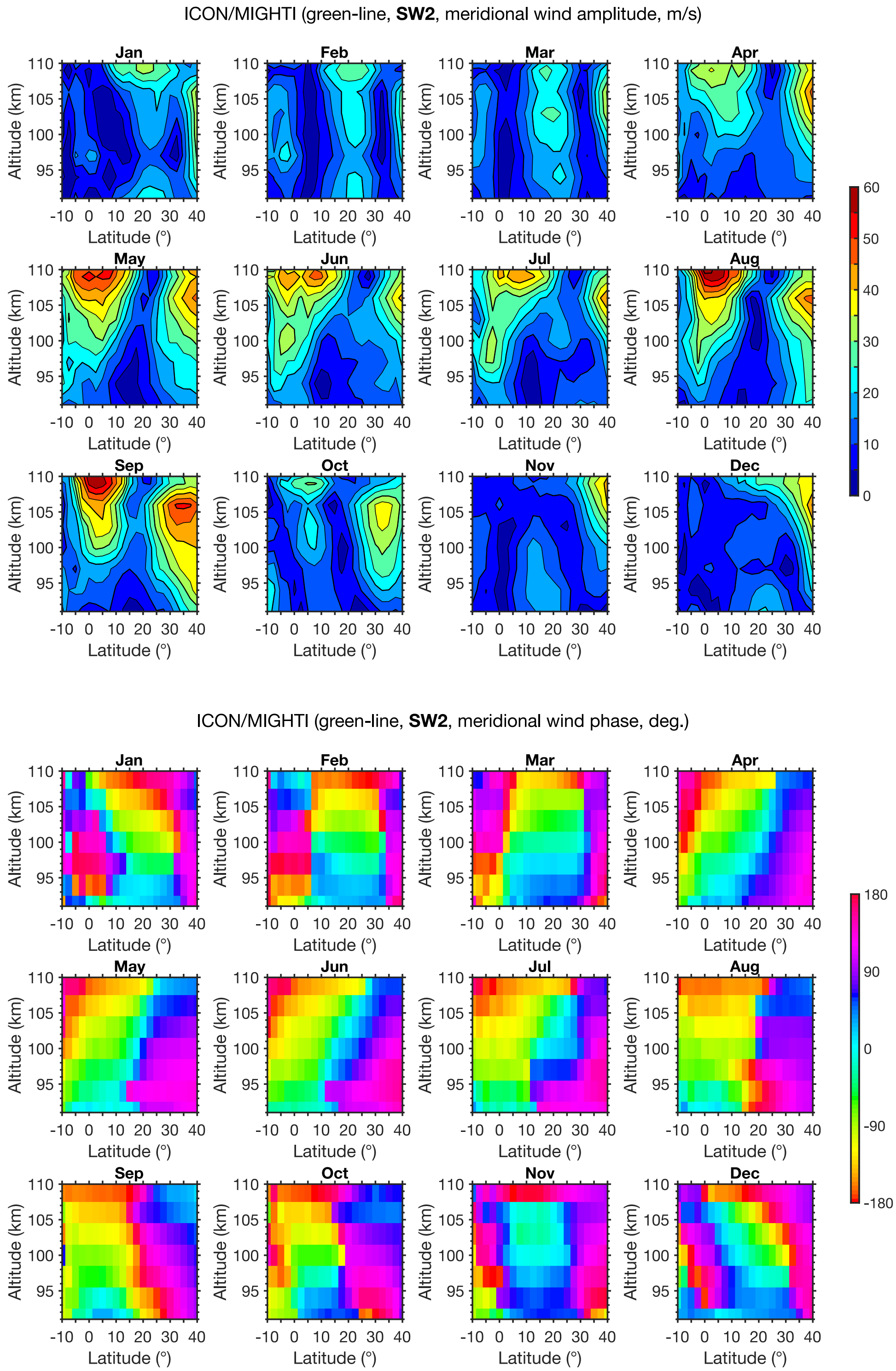

Figure 10. Amplitude (top 12 panels) and phase (bottom 12 panels) of the migrating semidiurnal tide (SW2) in the meridional wind in the lower thermosphere as derived from the v05 ICON/MIGHTI green-line data. The corresponding results for the zonal wind can be found in Figure S2 of Supporting Information.

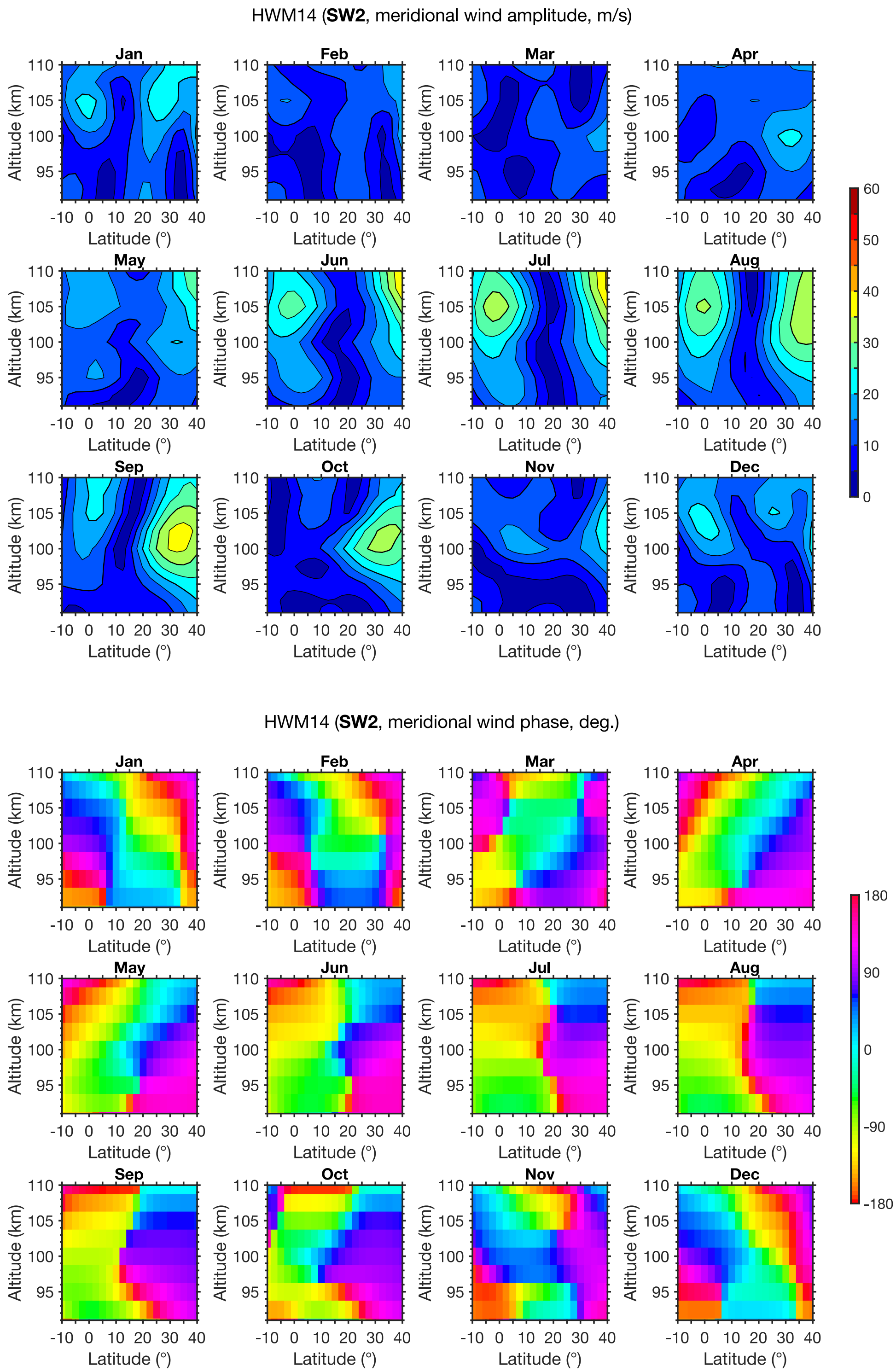

Figure 11. Same as Figure 10 but from Horizontal Wind Model 2014 (HWM14).

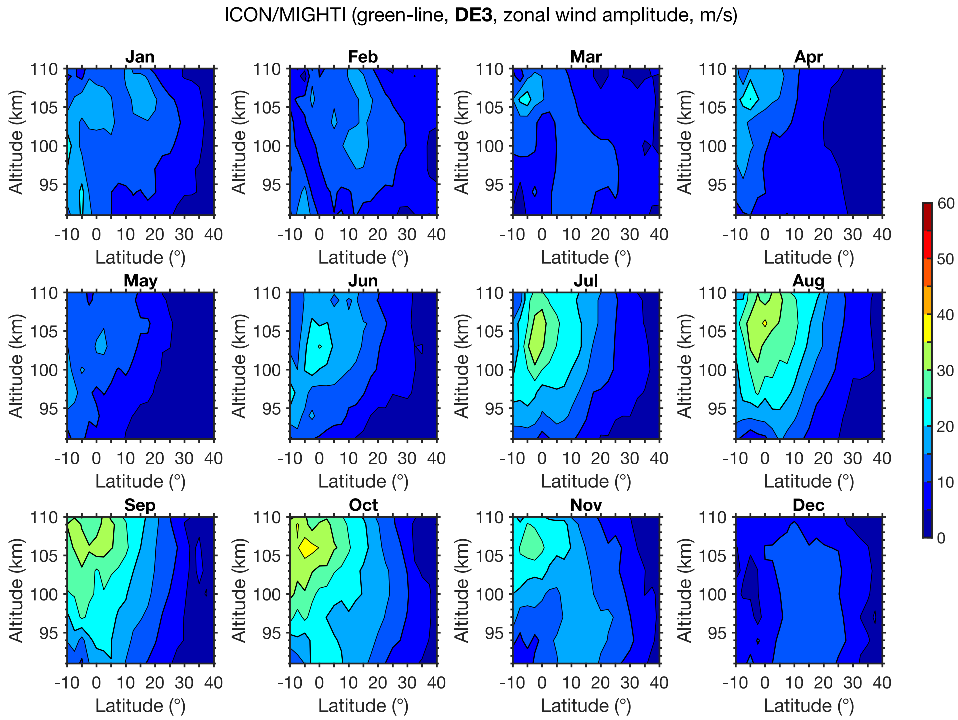

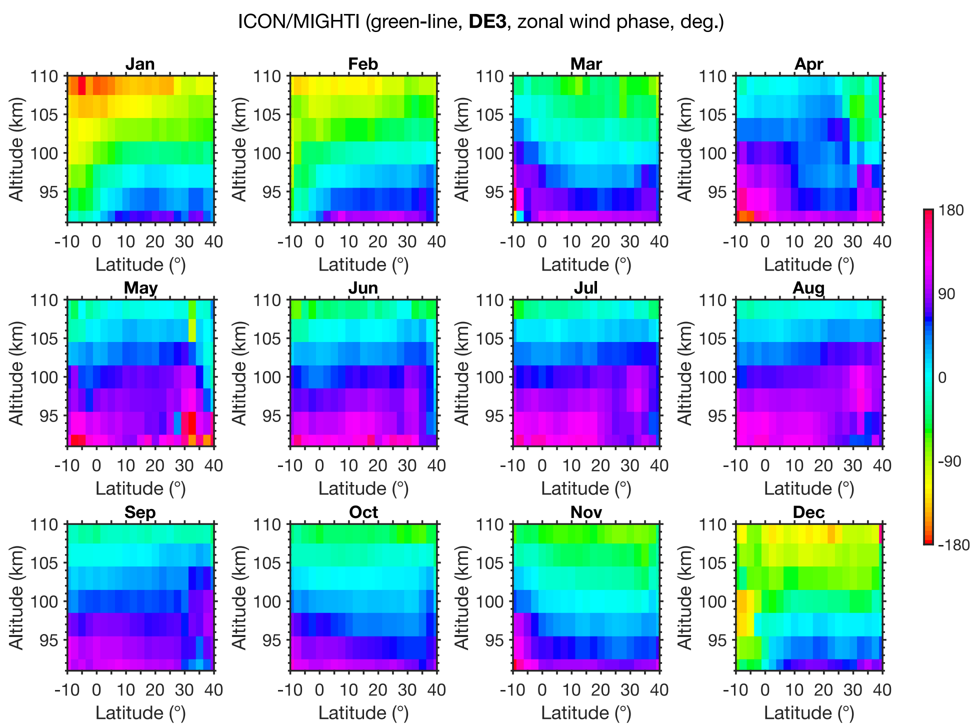

Figure 12. Amplitude (top 12 panels) and phase (bottom 12 panels) of the eastward-propagating diurnal tide with zonal wavenumber 3 (DE3) in the zonal wind in the lower thermosphere as derived from the v05 ICON/MIGHTI green-line data. The corresponding results for the meridional wind can be found in Figure S3 of Supporting Information.

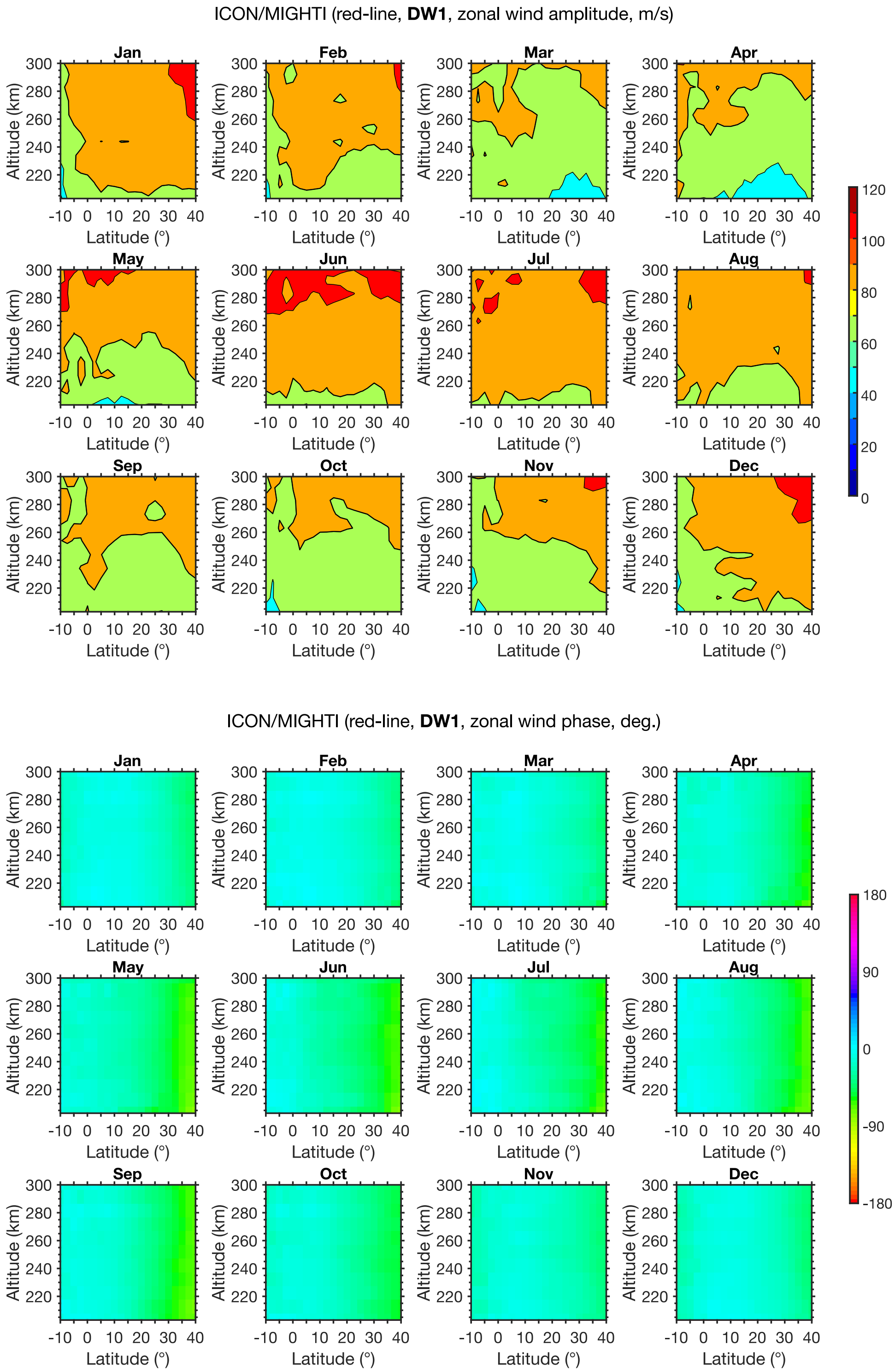

Figure 13. Amplitude (top 12 panels) and phase (bottom 12 panels) of the migrating diurnal tide (DW1) in the zonal wind in the middle thermosphere as derived from the v05 ICON/MIGHTI red-line data. The corresponding results for the migrating semidiurnal tide (SW2) can be found in Figure S4 of Supporting Information.

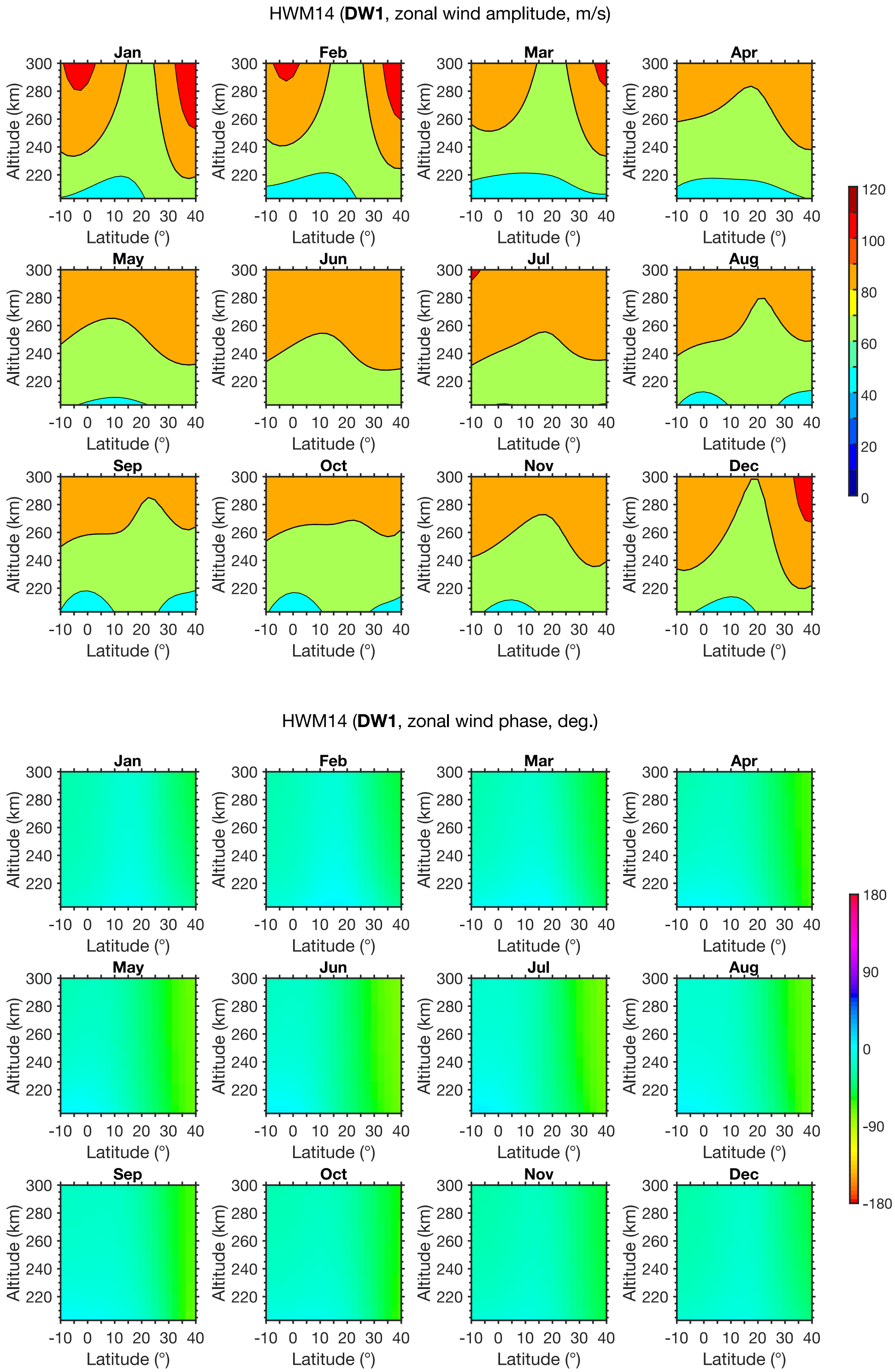

Figure 14. Same as Figure 13 but from Horizontal Wind Model 2014 (HWM14).

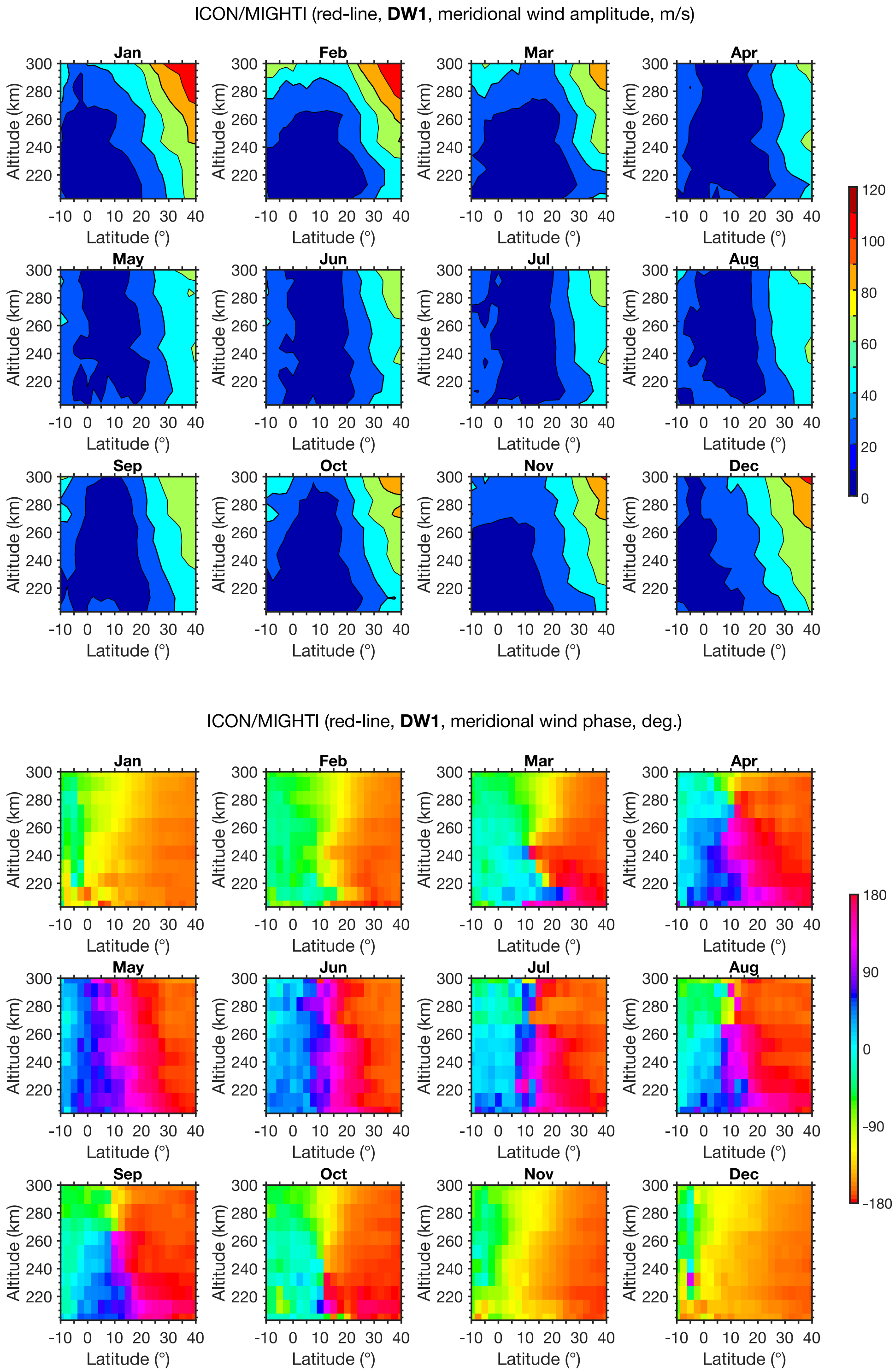

Figure 15. Same as Figure 13 but in the meridional wind. The corresponding results for the migrating semidiurnal tide (SW2) can be found in Figure S5 of Supporting Information.

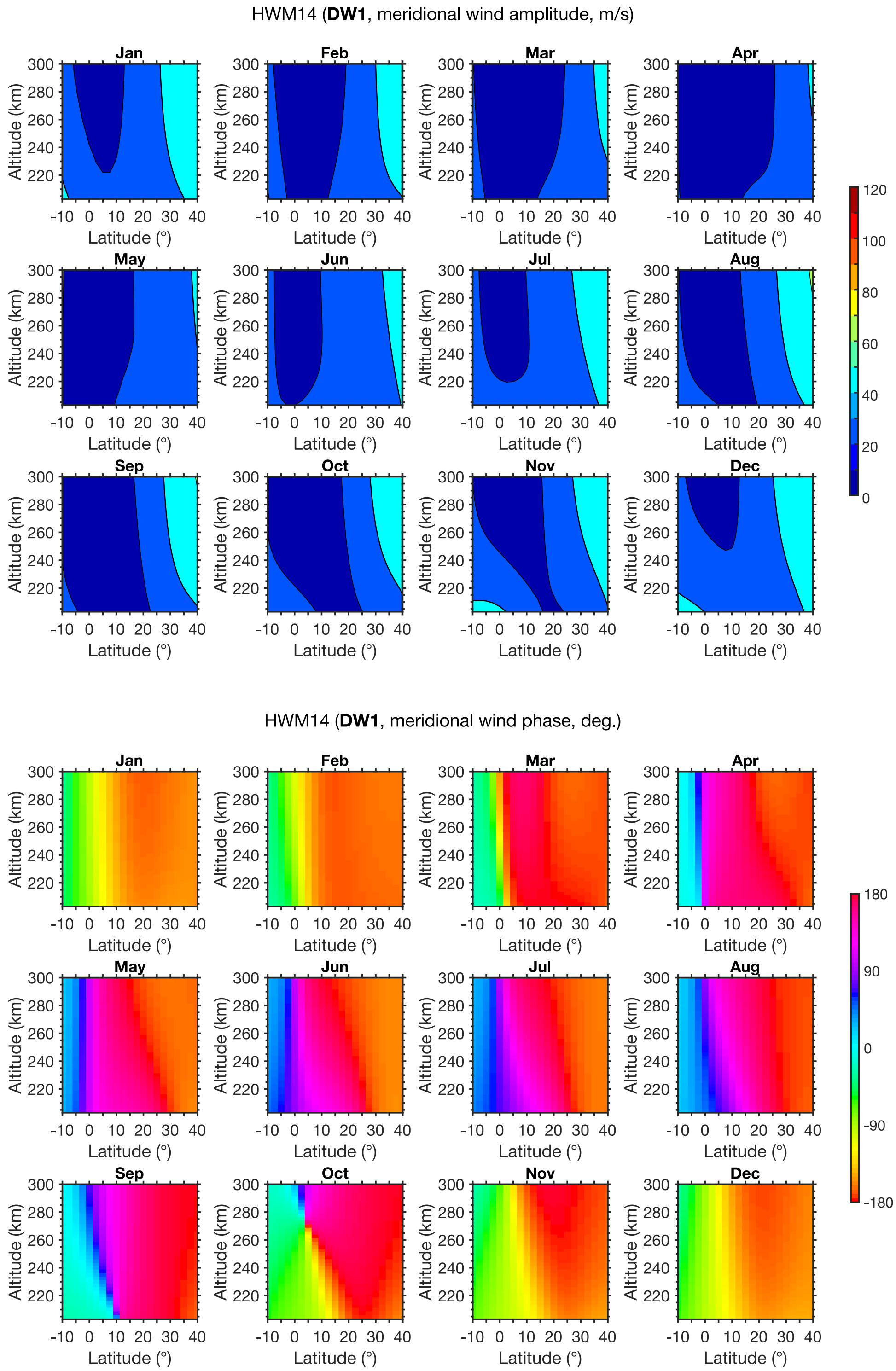

Figure 16. Same as Figure 14 but in the meridional wind.

4 Discussion

We have presented seasonal climatologies of the zonal-mean winds and tides derived from the v05 ICON/MIGHTI data, and compared the results with those from HWM14. Here we compare the ICON/MIGHTI results with those presented in earlier work based on other observations and models. Also, we discuss physical mechanisms behind some of the features observed in the ICON/MIGHTI winds, referring to previous theoretical studies.

Wang et al. (1997) created an empirical model of lower thermospheric winds (90–120 km) using the measurements from the wind imaging interferometer (WINDII; Shepherd et al., 1993) onboard UARS. They presented the zonal-mean zonal and meridional winds for different seasons, which can be compared with our ICON/MIGHTI results (Figures 2 and 4). S. P. Zhang et al. (2007) later analyzed an updated version of UARS/WINDII data and obtained similar results as Wang et al. (1997). The UARS/WINDII results showed a westward jet of 10–30 m/s over the equator at ∼100 km throughout the year. This is also seen in the ICON/MIGHTI results (Figure 2), as well as in HWM14 (Figure 3). It is noted that the UARS/WINDII data are already incorporated in HWM. The westward jet over the equator is considered to result from the westward momentum deposition by dissipating migrating (thus westward-propagating) tides (e.g., Miyahara, 1981, 1978; Lieberman & Hays, 1994; Jones Jr et al., 2014). Wang et al. (1997) and S. P. Zhang et al. (2007) noted that the equatorial westward jet is sandwiched by eastward jets centered around ±40° latitudes. The eastward jets were reported to be stronger in the summer hemisphere, with the magnitude of 30–40 m/s. The ICON/MIGHTI results (Figure 2) clearly capture the N.H. part of the eastward jets. The mechanism for the middle-latitude eastward jets is not well understood. The numerical work by Forbes et al. (1993) predicted that the equatorial westward jet induced by tidal dissipation is accompanied by eastward jets at higher latitudes. However, the eastward jets due to tidal dissipation are predicted to be much weaker than the westward jet, which agrees with neither ICON/MIGHTI nor UARS/WINDII observations. Besides tides, Miyoshi and Fujiwara (2006) numerically demonstrated that the momentum deposition by eastward-propagating equatorial Kelvin waves also plays a significant role for the zonal-mean zonal wind in the equatorial lower thermosphere. More studies are required to determine the relative importance of different waves to explain the observed westward and eastward jets.

The zonal-mean meridional wind in the lower thermosphere as derived from the ICON/MIGHTI data is generally weak (Figure 2), which is consistent with the UARS/WINDII results presented by Wang et al. (1997) as well as HWM14 (Figure 3). S. P. Zhang et al. (2007) noted that the zonal-mean meridional wind sometimes show a cell-like structure in the low latitude region, which is characterized by poleward winds on both sides of the equator at altitudes of 95–105 km and equatorward winds at 105–115 km. There is some hint of such a cell-like structure in the ICON/MIGHTI zonal-mean meridional wind (see, e.g., August–September), but it is not well resolved because of the small magnitude. The cell-like structure in the zonal-mean meridional wind in the lower thermosphere is sometimes found in numerical models and is considered to be driven by tidal dissipation (e.g., Miyahara et al., 1993; Forbes et al., 1993).

ICON/MIGHTI red-line measurements revealed seasonal climatologies of the zonal-mean zonal and meridional winds at 200–300 km (Figure 4). HWM14 reproduces the ICON/MIGHTI observations well for both the zonal and meridional components (Figure 5). HWM14 at this height range is well constrained by UARS/WINDII red-line winds as well as observations by ground-based Fabry-Perot interferometers. The zonal-mean meridional wind in the middle thermosphere is directed from the summer to the winter hemisphere, which is not surprising given the higher temperature and pressure in the summer hemisphere. The seasonal transition in the meridional circulation occurs in March and September. Using a numerical model, Roble et al. (1977) showed that the seasonal transition of the zonal-mean circulation takes place within a few weeks of equinox. Such an abrupt seasonal transition is not fully resolved in our monthly analysis. The zonal-mean zonal wind in the middle thermosphere arises mainly from the correlation between diurnal variations of pressure gradient and ion drag (Dickinson et al., 1975, 1977). That is, the wind is weaker on the dayside than the nightside as the ion drag is larger on the dayside due to higher plasma concentration. Since the wind in the middle thermosphere undergoes a diurnal cycle due to day-night pressure differences, an unbalance between the daytime and nighttime winds leads to the zonal-mean winds.

The three most dominant tidal components in the ICON/MIGHTI green-line winds are DW1, SW2 and DE3 (Figures 8, 10, 12). This is as expected from previous studies on tides in the lower thermosphere (e.g., Forbes et al., 2008; Oberheide et al., 2011). DW1 and SW2 are sun-synchronous, while DE3 is non-sun-synchronous. In the lower thermosphere, they consist mainly of upward-propagating modes, which can be seen from their downward phase propagation. They are driven by radiative heating through insolation of H_2O in the troposphere and O_3 in the stratosphere (e.g., Forbes, 1982b, 1982a) as well as by latent heating in the troposphere (Hagan & Forbes, 2002, 2003; X. Zhang et al., 2010a, 2010b). DW1 in the meridional wind, as derived from the ICON/MIGHTI observations, shows an amplitude maximum at 15–20°N at an altitude of 95–98 km (Figure 8). The results are consistent with those from UARS/WINDII (McLandress et al., 1996; S. P. Zhang et al., 2007) and TIMED/TIDI (Wu et al., 2008a). The amplitude is larger during the equinoxes than the solstices, which is well known from previous studies (e.g., Burrage et al., 1995; Xu et al., 2009). McLandress (2002b, 2002a) examined the mechanism for the semiannual variation of DW1 using a numerical model, and concluded that the change in the latitudinal shear of the zonal-mean zonal wind plays a leading role for the seasonal variation of DW1 in the lower thermosphere. HWM14 reproduces the semiannual variation of DW1 (Figure 9) but the model underestimates the amplitude in comparison not only with the ICON/MIGHTI results but also with the UARS/WINDII and TIMED/TIDI results (S. P. Zhang et al., 2007; Wu et al., 2008a). Previous studies reported that the amplitude of DW1 at low latitudes can change by a few tens of m/s from one year to the next (e.g., Burrage et al., 1995; Hagan et al., 1999). Variation associated with the quasi-biennial oscillation (QBO) of the equatorial atmosphere is an important part of the interannual variation of DW1 in the lower thermosphere, accounting for up to 10 m/s (e.g., Xu et al., 2009). The interannual variability of tides is not taken into account in the present study. Resolving the QBO effect would require a larger data set.

SW2 in the meridional wind, as derived from the ICON/MIGHTI observations, is relatively strong during May–September (Figure 10), which is consistent with the UARS/WINDII observations (S. P. Zhang et al., 2007). HWM14 reproduces the seasonal variation of SW2 but with somewhat smaller amplitude (Figure 11). The mechanism for the seasonal variation of SW2 is not well established. DE3 in the lower thermosphere has characteristics of a Kelvin wave (e.g., Forbes et al., 2003). In classical theory, a Kelvin wave travels eastward, and its zonal wind component has a Gaussian-shaped latitudinal profile with maximum amplitude over the equator (e.g., Forbes, 2000). The latitude and height structures of DE3 and its seasonal variation in the ICON/MIGHTI green-line zonal wind (Figure 12) are consistent with those from the UARS/WINDII (Forbes et al., 2003) and TIMED/TIDI observations (Oberheide et al., 2006; Wu et al., 2008b). As the zonal wind amplitude of

DE3 reaches its maximum in the equatorial dynamo region at 105–110 km, it has a significant impact on the equatorial zonal electric field and current (e.g., England et al., 2006; Fejer et al., 2008) as well as on the F-region plasma concentration (e.g., Immel et al., 2006; Lin et al., 2007). Despite the importance of DE3 in low-latitude ionosphere-thermosphere coupling, it is not included in HWM14 like other non-migrating tides.

DW1 in the middle thermosphere (Figures 13 and 15) is predominantly a vertically-trapped tidal mode that is excited by in-situ solar heating (e.g., Forbes, 1982b; Hagan et al., 2001). This contrasts with DW1 in the lower thermosphere (Figure 8), which is primarily an upward-propagating mode. The latitude and height structures of DW1 in the middle thermosphere are not well documented, particularly those based on observations. The simulation results by Hagan et al. (2001) showed that (1) the amplitude of DW1 at 200–300 km grows with height at all latitudes, (2) both zonal and meridional wind amplitudes are largest at high latitudes, (3) the meridional wind amplitude is vanishingly small over the equator but it increases with latitude, (4) the zonal wind amplitude does not depend strongly on latitude over the middle- and low-latitude regions, (5) both zonal and meridional wind phases do not depend strongly on height, (6) the zonal wind phase does not vary strongly with latitude, and (7) the meridional wind phase also does not vary strongly with latitude except that the phase reversal occurs at the equator. The ICON/MIGHTI results (Figures 13 and 15) are consistent with these numerical predictions.

Some previous studies have addressed a potential impact of the solar flux, mainly at the wavelengths of extreme ultraviolet (EUV), on neutral winds in the middle and upper thermosphere (e.g., Hedin et al., 1994). The ICON/MIGHTI observations examined in this paper are obtained during the period April 2020–March 2022. The mean value of the $F_{10.7}$ index (Tapping, 2013), which is often used as a proxy of the EUV flux, was 82.8 sfu (1 sfu = 10^{-22} W·m^{-2}·Hz^{-1}), with the minimum and maximum monthly values of 69.2 sft in May 2020 and 117.8 sfu in March 2022, respectively. We have ignored possible variations in the wind velocities associated with the change in the solar flux, as the ICON/MIGHTI data used in this study are not sufficient for evaluating the solar activity effect on the thermospheric winds. HWM14 also does not take into account the dependence of wind velocities on solar activity. Hedin et al. (1994) reported that although the solar flux significantly influences the temperature, the zonal-mean winds in the middle thermosphere do not strongly depend on solar activity. Hagan et al. (2001) noted in their simulation results that the solar flux has a marked effect on the temperature amplitude of DW1 in the middle thermosphere but not on the wind amplitudes. H. Liu et al. (2006) examined the effect of the solar flux on thermospheric winds (∼400 km) using the CHAMP accelerometer data. They found that the solar flux effect can be significant depending on the season and local time. The solar flux effect on tides is generally small below about 130 km, where tidal waves are mainly of lower atmospheric origin (Oberheide et al., 2009; Dhadly et al., 2018). More observational studies are required to establish the solar activity dependence of zonal-mean winds and tides in the thermosphere.

5 Conclusions

Monthly climatologies of quiet-time zonal-mean winds and tides are derived using the recently-released v05 of the ICON/MIGHTI thermopsheric wind measurements during April 2020–March 2022 at the altitude ranges 90–110 km and 200–300 km. Earlier versions of the ICON/MIGHTI wind data suffered from artificial baseline drifts that depend on local time. Thus, it was previously difficult to obtain reliable climatological estimates of zonal-mean winds and tides. The v05 data avoids this issue by the use of a renewed baseline calibration technique (Englert et al., 2023).

The ICON/MIGHTI results are compared with those from the latest version of HWM (i.e., HWM14) as well as previous studies. Salient features of zonal-mean winds and tides in the lower and middle thermosphere are in general agreement between ICON/MIGHTI and HWM14, including latitude and height structures and their seasonal variations. This provides a validation of the v05 ICON/MIGHTI data. HWM14 reproduces the zonal-mean zonal and meridional winds well in both the lower and middle thermosphere. However, HWM14 tends to underestimate tidal amplitude. Also, HWM14 does not include non-migrating tides such as DE3, which is especially important in the equatorial lower thermosphere. The latitude and height structures of DE3 and their seasonal variations in the ICON/MIGHTI green-line zonal wind are found to be consistent with those from the UARS/WINDII and TIMED/TIDI observations. The future improvement of HWM can benefit from the inclusion of the ICON/MIGHTI winds for better description of tides.

Open Research Section

The ICON/MIGHTI Level 2.2 product Cardinal Vector Winds (Version 5) is accessible from the ICON website `https://icon.ssl.berkeley.edu/Data`. The Hpo indices including Hp30 used in this study are available at the GFZ website `https://kp.gfz-potsdam.de/en/hp30-hp60/data`; see also data publication Matzka et al. (2022). The monthly F10.7 index is available at the website of the Canadian Space Weather Forecast Centre `https://spaceweather.gc.ca/forecast-prevision/solar-solaire/solarflux/sx-5-mavg-en.php`.

Acknowledgments

ICON was supported by NASA's Explorers Program through contracts NNG12FA45C and NNG12FA42I. Y.Y. was supported by the Deutsche Forschungsgemeinschaft (DFG) grant YA-574-3-1.

References

Aa, E., Zhang, S.-R., Wang, W., Erickson, P. J., Qian, L., Eastes, R., … others (2022). Pronounced suppression and X-pattern merging of equatorial ionization anomalies after the 2022 Tonga volcano eruption. *Journal of Geophysical Research: Space Physics*, *127*(6), e2022JA030527.

Burrage, M., Hagan, M., Skinner, W., Wu, D., & Hays, P. B. (1995). Long-term variability in the solar diurnal tide observed by HRDI and simulated by the GSWM. *Geophysical Research Letters*, *22*(19), 2641–2644.

Chang, L. C., Palo, S. E., & Liu, H.-L. (2011). Short-term variability in the migrating diurnal tide caused by interactions with the quasi 2 day wave. *Journal of Geophysical Research: Atmospheres*, *116*(D12).

Chau, J. L., Urco, J. M., Vierinen, J. P., Volz, R. A., Clahsen, M., Pfeffer, N., & Trautner, J. (2019). Novel specular meteor radar systems using coherent MIMO techniques to study the mesosphere and lower thermosphere. *Atmospheric Measurement Techniques*, *12*(4), 2113–2127.

Chen, Z., Liu, Y., Du, Z., Fan, Z., Sun, H., & Zhou, C. (2022). Validation of MIGHTI/ICON Atmospheric Wind Observations over China Region Based on Meteor Radar and Horizontal Wind Model (HWM14). *Atmosphere*, *13*(7), 1078.

Cullens, C. Y., Immel, T. J., Triplett, C. C., Wu, Y.-J., England, S. L., Forbes, J. M., & Liu, G. (2020). Sensitivity study for ICON tidal analysis. *Progress in Earth and Planetary Science*, *7*, 1–13.

Dhadly, M. S., Emmert, J. T., Drob, D. P., McCormack, J. P., & Niciejewski, R. J. (2018). Short-term and interannual variations of migrating diurnal and semidiurnal tides in the mesosphere and lower thermosphere. *Journal of Geophysical Research: Space Physics*, *123*(8), 7106–7123.

Dhadly, M. S., Englert, C. R., Drob, D. P., Emmert, J. T., Niciejewski, R., & Zawdie, K. A. (2021). Comparison of ICON/MIGHTI and TIMED/TIDI neutral wind measurements in the lower thermosphere. *Journal of Geophysical Research: Space Physics*, *126*(12), e2021JA029904.

Dickinson, R. E., Ridley, E., & Roble, R. (1975). Meridional circulation in the thermosphere I. Equinox conditions. *Journal of Atmospheric Sciences*, *32*(9), 1737–1754.

Dickinson, R. E., Ridley, E., & Roble, R. (1977). Meridional circulation in the thermosphere. II. Solstice conditions. *Journal of the Atmospheric Sciences*, *34*(1), 178–192.

Doornbos, E., Van Den Ijssel, J., Luhr, H., Forster, M., & Koppenwallner, G. (2010). Neutral density and crosswind determination from arbitrarily oriented multiaxis accelerometers on satellites. *Journal of Spacecraft and Rockets*, *47*(4), 580–589.

Drob, D., Emmert, J., Crowley, G., Picone, J., Shepherd, G., Skinner, W., ... others (2008). An empirical model of the Earth's horizontal wind fields: HWM07. *Journal of Geophysical Research: Space Physics*, *113*(A12).

Drob, D., Emmert, J., Meriwether, J. W., Makela, J. J., Doornbos, E., Conde, M., ... others (2015). An update to the Horizontal Wind Model (HWM): The quiet time thermosphere. *Earth and Space Science*, *2*(7), 301–319.

Emmert, J., Drob, D., Shepherd, G., Hernandez, G., Jarvis, M. J., Meriwether, J., ... Tepley, C. (2008). DWM07 global empirical model of upper thermospheric storm-induced disturbance winds. *Journal of Geophysical Research: Space Physics*, *113*(A11).

England, S. L., Maus, S., Immel, T., & Mende, S. (2006). Longitudinal variation of the E-region electric fields caused by atmospheric tides. *Geophysical Research*

Letters, *33*(21).

England, S. L., Meier, R., Frey, H. U., Mende, S. B., Stephan, A. W., Krier, C. S., … others (2021). First results from the retrieved column o/n2 ratio from the ionospheric connection explorer (icon): Evidence of the impacts of non-migrating tides. *Journal of Geophysical Research: Space Physics*, *126*(9), e2021JA029575.

Englert, C. R., Harlander, J., Brown, C., Meriwether, J., Makela, J., Castelaz, M., … Marr, K. (2012). Coincident thermospheric wind measurements using ground-based doppler asymmetric spatial heterodyne (dash) and fabry–perot interferometer (fpi) instruments. *Journal of Atmospheric and Solar-Terrestrial Physics*, *86*, 92–98.

Englert, C. R., Harlander, J. M., Brown, C. M., Marr, K. D., Miller, I. J., Stump, J. E., … others (2017). Michelson interferometer for global high-resolution thermospheric imaging (MIGHTI): instrument design and calibration. *Space Science Reviews*, *212*, 553–584.

Englert, C. R., Harlander, J. M., Marr, K. D., Harding, B. J., Makela, J. J., Fae, T., … Immel, T. J. (2023). Michelson Interferometer for Global High-resolution Thermospheric Imaging (MIGHTI) on-orbit wind observations: Data analysis and instrument performance. *Space Science Reviews, in press*.

Fejer, B. G., Jensen, J. W., & Su, S.-Y. (2008). Quiet time equatorial F region vertical plasma drift model derived from ROCSAT-1 observations. *Journal of Geophysical Research: Space Physics*, *113*(A5).

Forbes, J. M. (1982a). Atmospheric tide: 2. The solar and lunar semidiurnal components. *Journal of Geophysical Research: Space Physics*, *87*(A7), 5241–5252.

Forbes, J. M. (1982b). Atmospheric tides: 1. Model description and results for the solar diurnal component. *Journal of Geophysical Research: Space Physics*, *87*(A7), 5222–5240.

Forbes, J. M. (1995). Tidal and planetary waves. *The upper mesosphere and lower thermosphere: A review of experiment and theory*, *87*, 67–87.

Forbes, J. M. (2000). Wave coupling between the lower and upper atmosphere: case study of an ultra-fast Kelvin wave. *Journal of Atmospheric and Solar-Terrestrial Physics*, *62*(17-18), 1603–1621.

Forbes, J. M., Oberheide, J., Zhang, X., Cullens, C., Englert, C. R., Harding, B. J.,

... Immel, T. J. (2022). Vertical coupling by solar semidiurnal tides in the thermosphere from ICON/MIGHTI measurements. *Journal of Geophysical Research: Space Physics*, *127*(5), e2022JA030288.

Forbes, J. M., Roble, R. G., & Fesen, C. G. (1993). Acceleration, heating, and compositional mixing of the thermosphere due to upward propagating tides. *Journal of Geophysical Research: Space Physics*, *98*(A1), 311–321.

Forbes, J. M., Zhang, X., & Bruinsma, S. L. (2014). New perspectives on thermosphere tides: 2. Penetration to the upper thermosphere. *Earth, Planets and Space*, *66*(1), 1–11.

Forbes, J. M., Zhang, X., Heelis, R., Stoneback, R., Englert, C. R., Harlander, J. M., ... Immel, T. J. (2021). Atmosphere-ionosphere (A-I) coupling as viewed by ICON: Day-to-day variability due to planetary wave (PW)-tide interactions. *Journal of Geophysical Research: Space Physics*, *126*(6), e2020JA028927.

Forbes, J. M., Zhang, X., Palo, S., Russell, J., Mertens, C., & Mlynczak, M. (2008). Tidal variability in the ionospheric dynamo region. *Journal of Geophysical Research: Space Physics*, *113*(A2).

Forbes, J. M., Zhang, X., Talaat, E. R., & Ward, W. (2003). Nonmigrating diurnal tides in the thermosphere. *Journal of Geophysical Research: Space Physics*, *108*(A1).

Fuller-Rowell, T., Codrescu, M., Moffett, R., & Quegan, S. (1994). Response of the thermosphere and ionosphere to geomagnetic storms. *Journal of Geophysical Research: Space Physics*, *99*(A3), 3893–3914.

Fuller-Rowell, T., & Rees, D. (1980). A three-dimensional time-dependent global model of the thermosphere. *Journal of Atmospheric Sciences*, *37*(11), 2545–2567.

Fuller-Rowell, T., & Rees, D. (1981). A three-dimensional, time-dependent simulation of the global dynamical response of the thermosphere to a geomagnetic substorm. *Journal of Atmospheric and Terrestrial Physics*, *43*(7), 701–721.

Gasperini, F., Azeem, I., Crowley, G., Perdue, M., Depew, M., Immel, T. J., ... others (2021). Dynamical coupling between the low-latitude lower thermosphere and ionosphere via the nonmigrating diurnal tide as revealed by concurrent satellite observations and numerical modeling. *Geophysical Research Letters*, *48*(14), e2021GL093277.

Gasperini, F., Crowley, G., Immel, T. J., & Harding, B. J. (2022). Vertical wave coupling in the low-latitude Ionosphere-Thermosphere as revealed by concurrent ICON and COSMIC-2 Observations. *Space Science Reviews*, *218*(7), 55.

Geisler, J. (1967). A numerical study of the wind system in the middle thermosphere. *Journal of Atmospheric and Terrestrial Physics*, *29*(12), 1469–1482.

Hagan, M., Burrage, M., Forbes, J., Hackney, J., Randel, W., & Zhang, X. (1999). QBO effects on the diurnal tide in the upper atmosphere. *Earth, planets and space*, *51*, 571–578.

Hagan, M., & Forbes, J. (2002). Migrating and nonmigrating diurnal tides in the middle and upper atmosphere excited by tropospheric latent heat release. *Journal of Geophysical Research: Atmospheres*, *107*(D24), ACL–6.

Hagan, M., & Forbes, J. M. (2003). Migrating and nonmigrating semidiurnal tides in the upper atmosphere excited by tropospheric latent heat release. *Journal of Geophysical Research: Space Physics*, *108*(A2).

Hagan, M., Roble, R., & Hackney, J. (2001). Migrating thermospheric tides. *Journal of Geophysical Research: Space Physics*, *106*(A7), 12739–12752.

Harding, B. J., Chau, J. L., He, M., Englert, C. R., Harlander, J. M., Marr, K. D., … others (2021). Validation of ICON-MIGHTI thermospheric wind observations: 2. Green-line comparisons to specular meteor radars. *Journal of Geophysical Research: Space Physics*, *126*(3), e2020JA028947.

Harding, B. J., Makela, J. J., Englert, C. R., Marr, K. D., Harlander, J. M., England, S. L., & Immel, T. J. (2017). The MIGHTI wind retrieval algorithm: Description and verification. *Space Science Reviews*, *212*, 585–600.

Harding, B. J., Wu, Y.-J. J., Alken, P., Yamazaki, Y., Triplett, C. C., Immel, T. J., … Xiong, C. (2022). Impacts of the January 2022 Tonga volcanic eruption on the ionospheric dynamo: ICON-MIGHTI and Swarm observations of extreme neutral winds and currents. *Geophysical Research Letters*, *49*(9), e2022GL098577.

Harper, R. (1977). Tidal winds in the 100-to 200-km region at arecibo. *Journal of Geophysical Research*, *82*(22), 3243–3250.

Hays, P., Abreu, V. J., Dobbs, M. E., Gell, D. A., Grassl, H. J., & Skinner, W. R. (1993). The high-resolution doppler imager on the Upper Atmosphere Research Satellite. *Journal of Geophysical Research: Atmospheres*, *98*(D6), 10713–10723.

Hays, P., Killeen, T., & Kennedy, B. (1981). The Fabry-Perot interferometer on Dynamics Explorer. *Space Science Instrumentation*, *5*, 395–416.

He, M., Chau, J. L., Forbes, J. M., Zhang, X., Englert, C. R., Harding, B. J., … others (2021). Quasi-2-day wave in low-latitude atmospheric winds as viewed from the ground and space during January–March, 2020. *Geophysical Research Letters*, *48*(13), e2021GL093466.

Hedin, A. E., Biondi, M., Burnside, R., Hernandez, G., Johnson, R., Killeen, T., … others (1991). Revised global model of thermosphere winds using satellite and ground-based observations. *Journal of Geophysical Research: Space Physics*, *96*(A5), 7657–7688.

Hedin, A. E., Buonsanto, M., Codrescu, M., Duboin, M.-L., Fesen, C., Hagan, M., … Sipler, D. (1994). Solar activity variations in midlatitude thermospheric meridional winds. *Journal of Geophysical Research: Space Physics*, *99*(A9), 17601–17608.

Hedin, A. E., Fleming, E., Manson, A., Schmidlin, F., Avery, S., Clark, R., … others (1996). Empirical wind model for the upper, middle and lower atmosphere. *Journal of atmospheric and terrestrial physics*, *58*(13), 1421–1447.

Heelis, R. (2004). Electrodynamics in the low and middle latitude ionosphere: A tutorial. *Journal of Atmospheric and Solar-Terrestrial Physics*, *66*(10), 825–838.

Heelis, R., Chen, Y.-J., Depew, M., Harding, B. J., Immel, T. J., Wu, Y.-J., … others (2022). Topside plasma flows in the equatorial ionosphere and their relationships to f-region winds near 250 km. *Journal of Geophysical Research: Space Physics*, *127*(5), e2022JA030415.

Hocking, W., Fuller, B., & Vandepeer, B. (2001). Real-time determination of meteor-related parameters utilizing modern digital technology. *Journal of Atmospheric and Solar-Terrestrial Physics*, *63*(2-3), 155–169.

Immel, T. J., England, S., Mende, S., Heelis, R., Englert, C., Edelstein, J., … others (2018). The ionospheric connection explorer mission: Mission goals and design. *Space Science Reviews*, *214*, 1–36.

Immel, T. J., Harding, B. J., Heelis, R., Maute, A., Forbes, J. M., England, S. L., … others (2021). Regulation of ionospheric plasma velocities by thermospheric winds. *Nature geoscience*, *14*(12), 893–898.

Immel, T. J., Sagawa, E., England, S., Henderson, S., Hagan, M., Mende, S., ... Paxton, L. (2006). Control of equatorial ionospheric morphology by atmospheric tides. *Geophysical Research Letters*, *33*(15).

Jacchia, L. G. (1965). Static diffusion models of the upper atmosphere with empirical temperature profiles. In *Smithsonian Contributions to Astrophysics, Volume 8, Number 9* (pp. 215–257). Washington, D.C.: Smithsonian Institution.

Jiang, G., Xu, J., Wang, W., Yuan, W., Zhang, S., Yu, T., ... others (2018). A comparison of quiet time thermospheric winds between FPI observations and model calculations. *Journal of Geophysical Research: Space Physics*, *123*(9), 7789–7805.

Jones Jr, M., Forbes, J., Hagan, M., & Maute, A. (2014). Impacts of vertically propagating tides on the mean state of the ionosphere-thermosphere system. *Journal of Geophysical Research: Space Physics*, *119*(3), 2197–2213.

Kato, S. (2007). Thermosphere. In Y. Kamide & A. Chian (Eds.), *Handbook of the Solar-Terrestrial Environment* (pp. 222–245). Heidelberg, Germany: Springer Berlin Heidelberg. doi: 10.1007/978-3-540-46315-3_8

Killeen, T., Wu, Q., Solomon, S., Ortland, D., Skinner, W., Niciejewski, R., & Gell, D. (2006). TIMED Doppler Interferometer: Overview and recent results. *Journal of Geophysical Research: Space Physics*, *111*(A10).

Kohl, H., & King, J. (1967). Atmospheric winds between 100 and 700 km and their effects on the ionosphere. *Journal of Atmospheric and Terrestrial Physics*, *29*(9), 1045–1062.

Larsen, M. F. (2002). Winds and shears in the mesosphere and lower thermosphere: Results from four decades of chemical release wind measurements. *Journal of Geophysical Research: Space Physics*, *107*(A8), SIA–28.

Le, G., Liu, G., Yizengaw, E., & Englert, C. R. (2022). Intense equatorial electrojet and counter electrojet caused by the 15 January 2022 Tonga volcanic eruption: Space-and ground-based observations. *Geophysical Research Letters*, *49*(11), e2022GL099002.

Li, W., Chen, Y., Liu, L., Trondsen, T. S., Unick, C., Wyatt, D., ... others (2021). Variations of thermospheric winds observed by a Fabry–Pérot interferometer at Mohe, China. *Journal of Geophysical Research: Space Physics*, *126*(2), e2020JA028655.

Lieberman, R. S., & Hays, P. B. (1994). An estimate of the momentum deposition in the lower thermosphere by the observed diurnal tide. *Journal of atmospheric sciences*, *51* (20), 3094–3105.

Lin, C., Wang, W., Hagan, M. E., Hsiao, C., Immel, T., Hsu, M., . . . Liu, C. (2007). Plausible effect of atmospheric tides on the equatorial ionosphere observed by the FORMOSAT-3/COSMIC: Three-dimensional electron density structures. *Geophysical Research Letters*, *34* (11).

Lindzen, R. S., & Chapman, S. (1969). Atmospheric tides. *Space science reviews*, *10* (1), 3–188.

Liu, G., England, S. L., Lin, C. S., Pedatella, N. M., Klenzing, J. H., Englert, C. R., . . . Rowland, D. E. (2021). Evaluation of atmospheric 3-day waves as a source of day-to-day variation of the ionospheric longitudinal structure. *Geophysical research letters*, *48* (15), e2021GL094877.

Liu, H., Doornbos, E., & Nakashima, J. (2016). Thermospheric wind observed by GOCE: Wind jets and seasonal variations. *Journal of Geophysical Research: Space Physics*, *121* (7), 6901–6913.

Liu, H., Lühr, H., Watanabe, S., Köhler, W., Henize, V., & Visser, P. (2006). Zonal winds in the equatorial upper thermosphere: Decomposing the solar flux, geomagnetic activity, and seasonal dependencies. *Journal of Geophysical Research: Space Physics*, *111* (A7).

Liu, H.-L. (2014). WACCM-X simulation of tidal and planetary wave variability in the upper atmosphere. *Modeling the Ionosphere–Thermosphere System*, 181–199.

Liu, H.-L. (2016). Variability and predictability of the space environment as related to lower atmosphere forcing. *Space Weather*, *14* (9), 634–658.

Makela, J. J., Baughman, M., Navarro, L. A., Harding, B. J., Englert, C. R., Harlander, J. M., . . . Immel, T. J. (2021). Validation of ICON-MIGHTI thermospheric wind observations: 1. Nighttime red-line ground-based Fabry-Perot interferometers. *Journal of Geophysical Research: Space Physics*, *126* (2), e2020JA028726.

Makela, J. J., Meriwether, J. W., Ridley, A. J., Ciocca, M., & Castellez, M. W. (2012). Large-scale measurements of thermospheric dynamics with a multisite Fabry-Perot interferometer network: Overview of plans and results from midlatitude measurements. *International Journal of Geophysics*, *2012*.

Matzka, J., Stolle, C., Yamazaki, Y., Bronkalla, O., & Morschhauser, A. (2021). The geomagnetic Kp index and derived indices of geomagnetic activity. *Space Weather*, *19*(5), e2020SW002641.

McLandress, C. (2002a). The seasonal variation of the propagating diurnal tide in the mesosphere and lower thermosphere. Part II: The role of tidal heating and zonal mean winds. *Journal of the Atmospheric Sciences*, *59*(5), 907–922.

McLandress, C. (2002b). The seasonal variation of the propagating diurnal tide in the mesosphere and lower thermosphere. Part I: The role of gravity waves and planetary waves. *Journal of the Atmospheric Sciences*, *59*(5), 893–906.

McLandress, C., Shepherd, G. G., & Solheim, B. H. (1996). Satellite observations of thermospheric tides: Results from the Wind Imaging Interferometer on UARS. *Journal of Geophysical Research: Atmospheres*, *101*(D2), 4093–4114.

Meriwether, J. (2006). Studies of thermospheric dynamics with a Fabry–Perot interferometer network: A review. *Journal of Atmospheric and Solar-Terrestrial Physics*, *68*(13), 1576–1589.

Miyahara, S. (1978). Zonal mean winds induced by vertically propagating atmospheric tidal waves in the lower thermosphere. *Journal of the Meteorological Society of Japan. Ser. II*, *56*(2), 86–97.

Miyahara, S. (1981). Zonal mean winds induced by solar diurnal tides in the lower thermosphere. *Journal of the Meteorological Society of Japan. Ser. II*, *59*(3), 303–319.

Miyahara, S., Yoshida, Y., & Miyoshi, Y. (1993). Dynamic coupling between the lower and upper atmosphere by tides and gravity waves. *Journal of atmospheric and terrestrial physics*, *55*(7), 1039–1053.

Miyoshi, Y., & Fujiwara, H. (2006). Excitation mechanism of intraseasonal oscillation in the equatorial mesosphere and lower thermosphere. *Journal of Geophysical Research: Atmospheres*, *111*(D14).

Nystrom, V., Gasperini, F., Forbes, J. M., & Hagan, M. E. (2018). Exploring wave-wave interactions in a general circulation model. *Journal of Geophysical Research: Space Physics*, *123*(1), 827–847.

Oberheide, J. (2022). Day-to-day variability of the semidiurnal tide in the F-region ionosphere during the January 2021 SSW from COSMIC-2 and ICON. *Geophysical Research Letters*, *49*(17), e2022GL100369.

Oberheide, J., Forbes, J., Häusler, K., Wu, Q., & Bruinsma, S. (2009). Tropospheric tides from 80 to 400 km: Propagation, interannual variability, and solar cycle effects. *Journal of Geophysical Research: Atmospheres*, *114*(D1).

Oberheide, J., Forbes, J., Zhang, X., & Bruinsma, S. (2011). Climatology of upward propagating diurnal and semidiurnal tides in the thermosphere. *Journal of Geophysical Research: Space Physics*, *116*(A11).

Oberheide, J., Wu, Q., Killeen, T., Hagan, M., & Roble, R. (2006). Diurnal nonmigrating tides from TIMED Doppler Interferometer wind data: Monthly climatologies and seasonal variations. *Journal of Geophysical Research: Space Physics*, *111*(A10).

Okoh, D., Bounhir, A., Habarulema, J. B., Rabiu, B., Katamzi-Joseph, Z., Ojo, T., … Makela, J. J. (2022). Thermospheric neutral wind measurements and investigations across the African region–A review. *Atmosphere*, *13*(6), 863.

Park, J., Huba, J., Heelis, R., & Englert, C. (2021). Isolated peak of oxygen ion fraction in the post-noon equatorial F-region: ICON and SAMI3/WACCM-X. *Journal of Geophysical Research: Space Physics*, *126*(9), e2021JA029217.

Pfaff, R., Larsen, M., Abe, T., Habu, H., Clemmons, J., Freudenreich, H., … others (2020). Daytime dynamo electrodynamics with spiral currents driven by strong winds revealed by vapor trails and sounding rocket probes. *Geophysical research letters*, *47*(15), e2020GL088803.

Richmond, A. (1983). Thermospheric dynamics and electrodynamics. In R. L. Carovillano & J. M. Forbes (Eds.), *Solar-Terrestrial Physics: Principles and Theoretical Foundations* (pp. 523–607). Dordrecht, Netherlands: D. Reidel Publishing Co.

Richmond, A., Ridley, E., & Roble, R. (1992). A thermosphere/ionosphere general circulation model with coupled electrodynamics. *Geophysical Research Letters*, *19*(6), 601–604.

Rishbeth, H. (1998). How the thermospheric circulation affects the ionospheric F2-layer. *Journal of Atmospheric and Solar-Terrestrial Physics*, *60*(14), 1385–1402.

Roble, R., Dickinson, R. E., & Ridley, E. (1977). Seasonal and solar cycle variations of the zonal mean circulation in the thermosphere. *Journal of Geophysical Research*, *82*(35), 5493–5504.

Roble, R., Ridley, E. C., Richmond, A., & Dickinson, R. (1988). A coupled thermosphere/ionosphere general circulation model. *Geophysical Research Letters*, *15*(12), 1325–1328.

Salah, J., & Holt, J. (1974). Midlatitude thermospheric winds from incoherent scatter radar and theory. *Radio Science*, *9*(2), 301–313.

Shepherd, G. G., Thuillier, G., Gault, W., Solheim, B., Hersom, C., Alunni, J., ... others (1993). WINDII, the wind imaging interferometer on the upper atmosphere research satellite. *Journal of Geophysical Research: Atmospheres*, *98*(D6), 10725–10750.

Shiokawa, K., Katoh, Y., Satoh, M., Ejiri, M., Ogawa, T., Nakamura, T., ... Wiens, R. (1999). Development of optical mesosphere thermosphere imagers (OMTI). *Earth, Planets and Space*, *51*, 887–896.

Spencer, N., Wharton, L., Carignan, G., & Maurer, J. (1982). Thermosphere zonal winds, vertical motions and temperature as measured from Dynamics Explorer. *Geophysical Research Letters*, *9*(9), 953–956.

Sutton, E. K., Nerem, R. S., & Forbes, J. M. (2007). Density and winds in the thermosphere deduced from accelerometer data. *Journal of Spacecraft and Rockets*, *44*(6), 1210–1219.

Tang, Q., Zhou, Y., Du, Z., Zhou, C., Qiao, J., Liu, Y., & Chen, G. (2021). A comparison of meteor radar observation over China region with horizontal wind model (HWM14). *Atmosphere*, *12*(1), 98.

Tapping, K. (2013). The 10.7 cm solar radio flux (F10. 7). *Space weather*, *11*(7), 394–406.

Triplett, C. C., Harding, B. J., Wu, Y.-J. J., England, S., Englert, C. R., Makela, J. J., ... Immel, T. (2023). Large-scale gravity waves in daytime ICON-MIGHTI data from 2020. *Space Science Reviews*, *219*(1), 3.

Truskowski, A. O., Forbes, J. M., Zhang, X., & Palo, S. E. (2014). New perspectives on thermosphere tides: 1. Lower thermosphere spectra and seasonal-latitudinal structures. *Earth, Planets and Space*, *66*, 1–17.

Wang, D., McLandress, C., Fleming, E., Ward, W., Solheim, B., & Shepherd, G. (1997). Empirical model of 90–120 km horizontal winds from wind-imaging interferometer green line measurements in 1992–1993. *Journal of Geophysical Research: Atmospheres*, *102*(D6), 6729–6745.

Wu, Q., Ortland, D., Killeen, T., Roble, R., Hagan, M., Liu, H.-L., ... Niciejewski, R. (2008a). Global distribution and interannual variations of mesospheric and lower thermospheric neutral wind diurnal tide: 1. Migrating tide. *Journal of Geophysical Research: Space Physics*, *113*(A5). doi: https://doi.org/10.1029/2007JA012542

Wu, Q., Ortland, D., Killeen, T., Roble, R., Hagan, M., Liu, H.-L., ... Niciejewski, R. (2008b). Global distribution and interannual variations of mesospheric and lower thermospheric neutral wind diurnal tide: 2. Nonmigrating tide. *Journal of Geophysical Research: Space Physics*, *113*(A5). doi: https://doi.org/10.1029/2007JA012543

Xu, J., Smith, A., Liu, H.-L., Yuan, W., Wu, Q., Jiang, G., ... Franke, S. (2009). Seasonal and quasi-biennial variations in the migrating diurnal tide observed by Thermosphere, Ionosphere, Mesosphere, Energetics and Dynamics (TIMED). *Journal of Geophysical Research: Atmospheres*, *114*(D13).

Yamazaki, Y., Arras, C., Andoh, S., Miyoshi, Y., Shinagawa, H., Harding, B., ... Stolle, C. (2022). Examining the wind shear theory of sporadic E with ICON/MIGHTI winds and COSMIC-2 radio occultation data. *Geophysical Research Letters*, *49*(1), e2021GL096202.

Yamazaki, Y., Harding, B., Stolle, C., & Matzka, J. (2021). Neutral wind profiles during periods of eastward and westward equatorial electrojet. *Geophysical Research Letters*, *48*(11), e2021GL093567.

Yamazaki, Y., Matzka, J., Stolle, C., Kervalishvili, G., Rauberg, J., Bronkalla, O., ... Jackson, D. (2022). Geomagnetic activity index Hpo. *Geophysical Research Letters*, *49*(10), e2022GL098860.

Yiğit, E., Dhadly, M., Medvedev, A. S., Harding, B. J., Englert, C. R., Wu, Q., & Immel, T. J. (2022). Characterization of the Thermospheric Mean Winds and Circulation during Solstice using ICON/MIGHTI Observations. *Journal of Geophysical Research: Space Physics*, *127*(11), e2022JA030851.

Yiğit, E., & Medvedev, A. S. (2015). Internal wave coupling processes in Earth's atmosphere. *Advances in Space Research*, *55*(4), 983–1003.

Zhang, R., Liu, L., Ma, H., Chen, Y., & Le, H. (2022). ICON observations of equatorial ionospheric vertical ExB and field-aligned plasma drifts during the 2020–2021 SSW. *Geophysical Research Letters*, *49*(16), e2022GL099238.

Zhang, S. P., McLandress, C., & Shepherd, G. G. (2007). Satellite observations of mean winds and tides in the lower thermosphere: 2. Wind Imaging Interferometer monthly winds for 1992 and 1993. *Journal of Geophysical Research: Atmospheres*, *112*(D21).

Zhang, X., Forbes, J. M., & Hagan, M. E. (2010a). Longitudinal variation of tides in the MLT region: 1. Tides driven by tropospheric net radiative heating. *Journal of Geophysical Research: Space Physics*, *115*(A6).

Zhang, X., Forbes, J. M., & Hagan, M. E. (2010b). Longitudinal variation of tides in the MLT region: 2. Relative effects of solar radiative and latent heating. *Journal of Geophysical Research: Space Physics*, *115*(A6).